CONVERSION MODE PHOTON ANALYSIS USING THE ALPHA MAGNETIC SPECTROMETER (AMS-02)

A THESIS SUBMITTED TO
THE GRADUATE SCHOOL OF NATURAL AND APPLIED SCIENCES
OF
MIDDLE EAST TECHNICAL UNIVERSITY

BY

EMİRHAN POSTACI

IN PARTIAL FULFILLMENT OF THE REQUIREMENTS
FOR
THE DEGREE OF MASTER OF SCIENCE
IN
PHYSICS

JULY 2014

Approval of the thesis:

CONVERSION MODE PHOTON ANALYSIS USING THE ALPHA MAGNETIC SPECTROMETER (AMS-02)

submitted by **EMİRHAN POSTACI** in partial fulfillment of the requirements for the degree of **Master of Science in Physics Department, Middle East Technical University** by,

Prof. Dr. Canan Özgen
Dean, Graduate School of **Natural and Applied Sciences** _______________

Prof. Dr. Mehmet T. Zeyrek
Head of Department, **Physics** _______________

Assoc. Prof. Dr. M. Bilge Demirköz
Supervisor, **Physics Department, METU** _______________

Examining Committee Members:

Prof. Dr. Mehmet T. Zeyrek
Physics Department, METU _______________

Assoc. Prof. Dr. M. Bilge Demirköz
Physics Department, METU _______________

Prof. Dr. Osman Yılmaz
Physics Department, METU _______________

Prof. Dr. Gürsevil Turan
Physics Department, METU _______________

Prof. Dr. Şakir Ayık
Physics Department, Tennessee Technological University _______________

Date: _______________

I hereby declare that all information in this document has been obtained and presented in accordance with academic rules and ethical conduct. I also declare that, as required by these rules and conduct, I have fully cited and referenced all material and results that are not original to this work.

Name, Last Name: EMİRHAN POSTACI

Signature :

ABSTRACT

CONVERSION MODE PHOTON ANALYSIS USING THE ALPHA MAGNETIC SPECTROMETER (AMS-02)

Postacı, Emirhan
M.S., Department of Physics
Supervisor : Assoc. Prof. Dr. M. Bilge Demirköz

July 2014, 54 pages

The Alpha Magnetic Spectrometer (AMS-02) is a particle physics detector operating as an external module on the International Space Station (ISS). It is designed to search for antimatter and dark matter by measuring cosmic ray composition and flux. Dark matter does not interact electromagnetically, so cannot be detected directly with optical instruments. A strong candidate of dark matter is the lightest supersymmetric particle which can annihilate into the Standard Model particles, called the neutralino. If neutralinos annihilate in the galactic halo, they could result in an excess of particles that can be detected by the AMS-02. Any peaks in the positron, antiproton, or photon spectrum could signal the presence of neutralinos, but would need to be distinguished from other complex astrophysical signals. Photon analysis can be done in two ways: calorimetric mode and conversion mode. In the calorimetric mode of photon analysis, photons leave no trace in subdetectors down to the ECAL. In the conversion mode, photons which are converted to electron-positron pairs in the upper parts of the AMS-02 are studied. This thesis outlines the study of conversion mode photon analysis above 100 GeV energy.

Keywords: Alpha Magnetic Spectrometer, AMS-02, Dark Matter, Weakly Interacting Massive Particles, WIMP, Conversion Mode, Photon

ÖZ

ALFA MANYETİK SPEKTROMETRESİ (AMS-02) İLE DÖNÜŞÜM MODUNDA FOTON ANALİZİ

Postacı, Emirhan
Yüksek Lisans, Fizik Bölümü
Tez Yöneticisi : Doç. Dr. M. Bilge Demirköz

Temmuz 2014 , 54 sayfa

Alfa Manyetik Spektrometresi (AMS-02), Uluslararası Uzay İstasyonu üzerinde harici bir modül olarak faaliyet gösteren bir parçacık fiziği dedektörüdür. Kozmik ışınların içeriğini ve akısını ölçerek karanlık madde ve anti madde aramak için tasarlanmıştır. Karanlık madde elektromanyetik etkileşme yapmadığı için optik enstrümanlar ile tespit edilemez. Karanlık madde olmaya güçlü bir aday, nötralino denilen, Standart Model parçacıklarına bozuşma olasılığı olan bir en hafif süpersimetrik parçacıktır. Eğer nötralinolar galaktik halede bozunursa AMS-02 tarafından gözlemlenebilen parçacıklarda bir fazlalık meydana getirebilir. Pozitron, anti proton veya foton tayfındaki herhangi bir fazlalık, nötralinonun varlığına bir işaret olabilir ama alacağımız sinyalin diğer karmaşık astrofiziksel sinyallerden ayırt edilmesi gerekir. Foton analizi iki şekilde yapılabilir: kalorimetrik mod ve dönüşüm modu. Kalorimetrik modda dedektörün en altında yer alan elektromanyetik kalorimetreye gelene kadar iz bırakmayan fotonlar incelenir. Dönüşüm modunda ise dedektörün üst kısımlarında elektron pozitron çiftine dönüşen fotonlar incelenir. Bu tez 100 GeV üzeri enerjilerde dönüşüm modunda foton analizi çalışmasını özetler.

Anahtar Kelimeler: Alfa Manyetik Spektrometresi, AMS-02, Karanlık Madde, Zayıf Etkileşen Devasa Parçacık, WIMP, Dönüşüm Modu, Foton

To my family

ACKNOWLEDGMENTS

I would like to express my special appreciation and thanks to my supervisor Prof. Bilge Demirköz for her guidance and patience starting from my undergraduate years. I have greatly benefited from her knowledge and experience. Her encouragement helped me very much while writing this thesis.

I would like to thank Prof. Ting who made AMS possible for me. I would also like to thank all the AMS Collaboration members I know, who helped me during the period that I stayed at CERN.

I would also like thank my colleagues Tansu Daylan, Cenk Türkoğlu, and Emre Ergeçen both for their help for improving my analysis, and their friendship. I will not forget the times we had both at METU and at CERN. I would also like to thank Dilek Kızılören, Ayşenur Gencer, and Ramazan Uzel for their contribution in the group meetings.

I would like to thank my friends Murat Öztürk and Elif Sarıgül who were with me throughout the Master's. We had much fun even in the stressful course taking period.

My special thanks go to my parents Reşide and Veysel, and my sisters Şebnem and Umut. They all believed and supported me. None of this would be possible without them.

Last but not least, I wish to thank Selen Saatci who gives me the power to go on in difficult times. Life would be so meaningless without her love. I also appreciate her help in the writing process of this thesis.

This work is partially supported by Turkish Atomic Energy Agency (TAEK) under the grant agreement 2012TAEKCERN-A5.H2.P1.01-20, and by the Marie Curie Career Integration Grants (CIG) under the grant agreement PCIG10-GA-2011-304264.

TABLE OF CONTENTS

LIST OF TABLES

TABLES

LIST OF FIGURES

FIGURES

LIST OF ABBREVIATIONS

ACC	Anticoincidence Counters
AMS	Alpha Magnetic Spectrometer
ATLAS	A Toroidal LHC Apparatus
BDT	Boosted Decision Tree
CAST	CERN Axion Solar Telescope
CERN	The European Organization for Nuclear Research
CMB	Cosmic microwave background
CMS	Compact Muon Solenoid
COBE	Cosmic Background Explorer
ECAL	Electromagnetic Calorimeter
ESA	European Space Agency
ISS	International Space Station
LHC	Large Hadron Collider
LNGS	Gran Sasso National Laboratory
LSP	Lightest supersymmetric particle
MC	Monte Carlo
MET	Missing transverse energy
MIP	Minimum ionizing particle
NASA	National Aeronautics and Space Administration
NGC	New General Catalogue of Nebulae and Clusters of Stars
PAMELA	a Payload for Antimatter Matter Exploration and Light-nuclei Astrophysics
PMT	Photomultiplier
QCD	Quantum Chromodynamics
RICH	Ring Imaging Čerenkov Detector
SAA	South Atlantic Anomaly
SM	Standard Model
SUSY	Supersymmetry
TOF	Time of Flight System

TR	Transition radiation
TRD	Transition Radiation Detector
WIMP	Weakly interacting massive particle
WMAP	Wilkinson Microwave Anisotropy Probe

CHAPTER 1

INTRODUCTION

The Alpha Magnetic Spectrometer (AMS-02) is a general purpose astroparticle physics experiment that was installed on the International Space Station (ISS) on the 19th of May, 2011, and has been taking cosmic-ray data since. Orbiting the Earth on the ISS at an altitude of about $300\ km$, AMS-02 is studying the composition of primary cosmic rays with an unprecedented accuracy of one part in 10 billion particles, exploring a new frontier in the field of particle physics. AMS-02 searches for primordial antimatter and a dark matter signature. AMS-02 measures the cosmic-ray spectrum for charged particles and photons, as well as for primary elements up to Fe. AMS-02 determines the momentum, the charge, the velocity and the energy of a particle using a permanent magnet and several subdetectors. AMS-02 allows for the measurement of momentum up to $3\ TeV/nucleon$ and charge of the particle by reconstructing the particle's curvature in the magnetic field. High energy photons which convert to e^+e^- pairs in the AMS-02 volume can also be identified and their energy, determined. The energy spectra of cosmic particles such as positrons, antiprotons, and photons can contain dark matter annihilation signatures in the galactic halo. AMS-02 measured over 50 billion particles for 1125 days as of the 18th of June, 2014, and it is going to operate until the end of the ISS mission which has been approved until 2024. AMS-02 published the first results about positron fraction in the Physical Review Letters using 8% of the total expected data [10]. Figure 1.1 shows AMS-02 subsystems and support structures.

In the AMS-02 collaboration, the analysis effort has been organized into two groups named Group Alpha and Group A, which independently work on each analysis topic

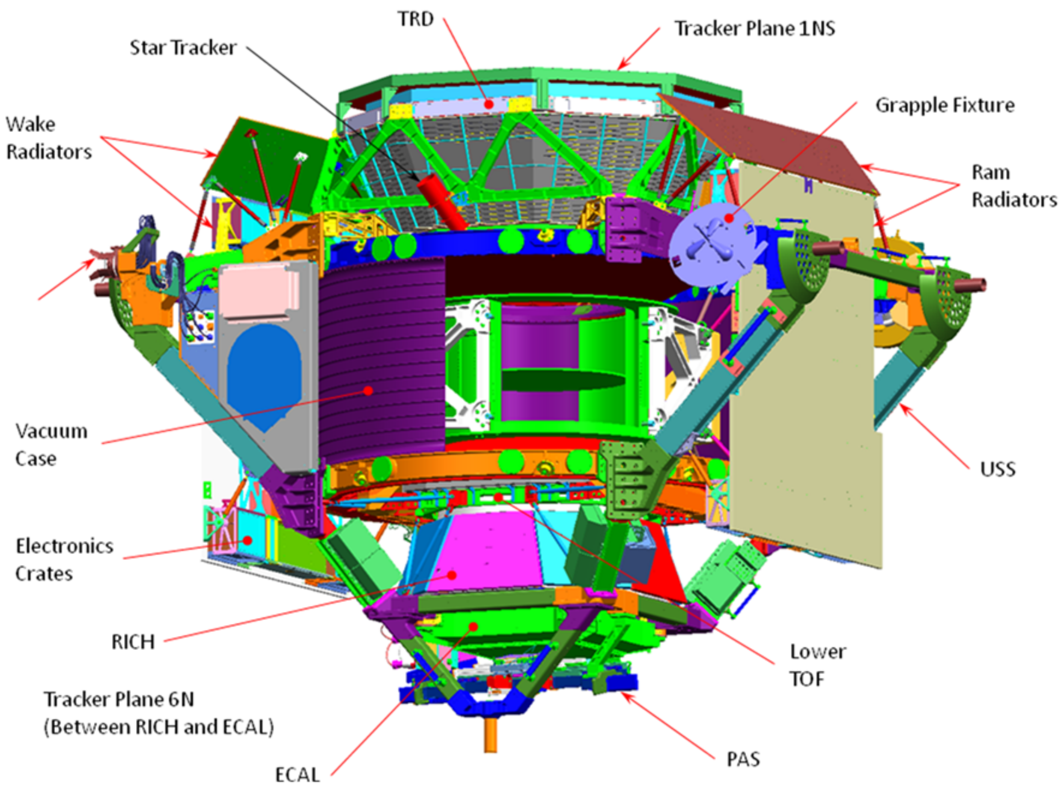

Figure 1.1: An overview of each of the AMS-02 subsystems and support structures [48].

before revealing their results at a designated collaboration meeting. Before publishing an analysis paper, the work and the results are cross-checked, sometimes based on different analysis techniques. Only when a consensus is reached, the analysis is concluded and the progress reported in physics journal. The METU-AMS team is part of the Alpha analysis effort along with MIT, Hawaii, LAPP-Annecy, Grenoble, Academia Sinica, IHEP-Beijing, Geneva and CIEMAT-Madrid groups.

This thesis outlines a conversion mode analysis for photon data collected by AMS-02. A sharp feature in the photon spectrum could be a strong signal of dark matter annihilation in the galactic halo. Therefore, this thesis first focuses on the theoretical predictions and the experimental search for dark matter in Chapter 2. Then, an overview of AMS-02 detector and current published results will be presented in Chapter 3. In Chapter 4, the analysis procedure will be explained in detail. Finally a brief conclusion will be given in Chapter 5.

CHAPTER 2

SEARCH FOR DARK MATTER

In this chapter, first, observational evidences for dark matter will be reviewed. Then, particle nature of dark matter, and the detection mechanism will be presented. Finally, electron-positron pair production mechanism will be discussed which is crucial for the author's analysis that will be explained later.

2.1 Observational Evidence

In 1933, Swiss astrophysicist Fritz Zwicky investigated the dispersion speed of a small group of seven galaxies in the Coma Cluster. Zwicky's goal was to calculate the total mass of the cluster, and he observed a discrepancy between the luminous mass and the dynamical mass measured by using the virial theorem. The dispersion speed of these galaxies was surprisingly lower than expected [51]. The conclusion Zwicky made pointed to the existence of extra mass. Since this extra mass must have been non-luminous, he named it dark matter.

After Zwicky's pioneering work, the next evidence for dark matter was presented by Vera Rubin in 1970. Rubin measured the velocity curve of spiral galaxies with a high precision spectrograph [45]. Rubin found out that most stars have approximately same orbital speeds in spiral galaxies, i.e., rotational curves of the galaxies are flat [44]. It was unexpected that galaxies do not have a Keplerian velocity decrease at large radius. Rubin concluded that non-luminous matter must exist beyond the visible galaxy. This work also suggests that dark matter must have a halo structure. A halo contribution must be added to obtain the observed flat rotation curve which can be seen in Figure 2.1. In other words, if there was no dark matter, not only would the average rotational velocity be lower on average, the profile would also be different.

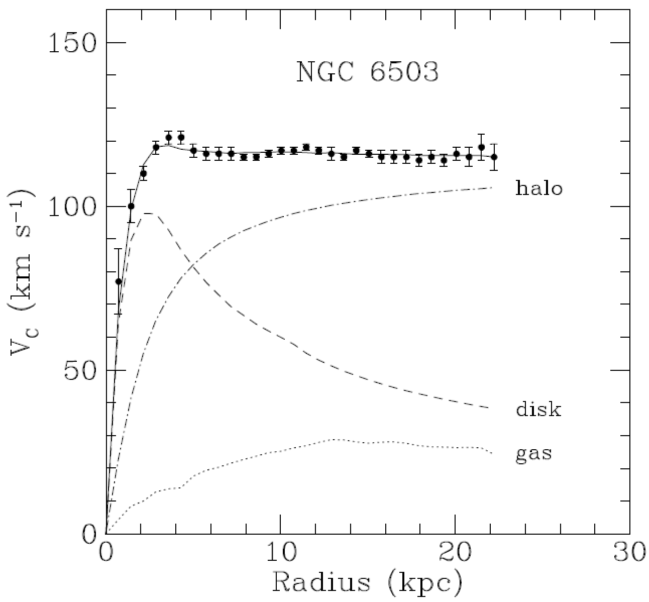

Figure 2.1: Rotation curve versus radius of NGC 6503 and contribution from various components of the galaxy. The dashed, dotted, and dash-dotted lines are the visible components, the gas, and the dark matter halo, respectively. Adding the dark halo contribution to Keplerian decrease, the measured flat rotation curve can be deduced [15].

1E 0657-558 ($z = 0.296$) cluster which is also known as the Bullet Cluster is considered as the strongest observational evidence for the existence of dark matter. The Bullet Cluster consists of two colliding clusters of galaxies which is shown in Figure 2.2. A weak lensing study shows that the gravitational potential traces the distribution of mass in the galaxy. Superimposed mass density contours which can be seen in Figure 2.2 in green shows the gravitational centers of the galaxy which is not in the same region as baryonic component of the galaxy. As two clusters collide, since the baryonic mass component has friction, it emits X-rays and slows down, while dark matter which is frictionless continues on its path with nearly constant velocity. At a statistical significance of 8σ, the spatial difference between the center of the total mass and the center of the baryonic mass peaks cannot be explained by modified gravitation theories. Hence, this study strongly indicates that the most of the matter in the system is unseen [28].

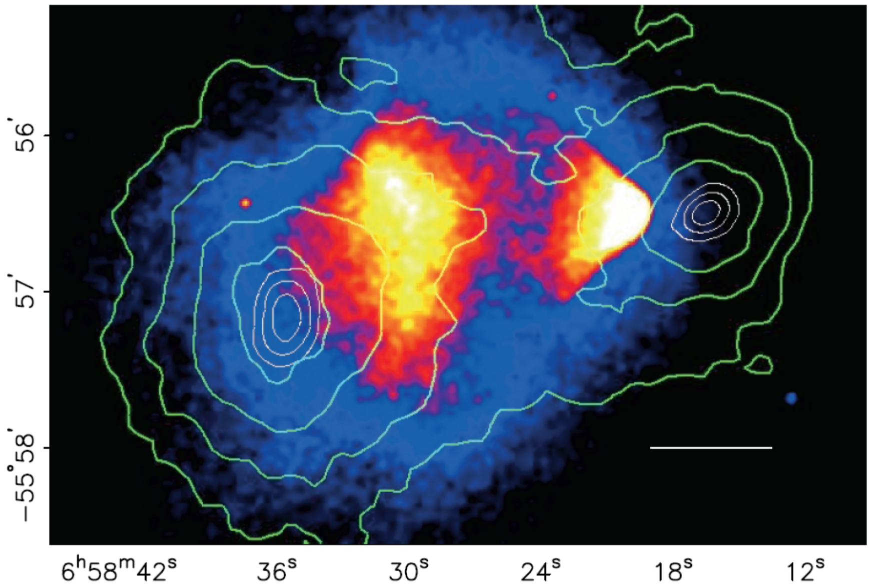

Figure 2.2: X-ray image of the Bullet Cluster by Chandra X-ray Observatory is in blue, red, and yellow. Superimposed mass density contours derived from the gravitational lensing effect are shown in green. Right ascension (x-axis) units are hours, minutes, and seconds, and declination (y-axis) units are degrees, and arcminutes [28].

Cosmic microwave background (CMB) radiation is a thermal radiation which fills the Universe CMB was discovered by Woodrow Wilson and Arno Penzias in 1963. Since then, more accurate measurements have been done. NASA Cosmic Background Explorer (COBE) measured the residual temperature as $2.726\ K$ in 1992, and detected the anisotropies for the first time [21]. Then, the Wilkinson Microwave Anisotropy Probe (WMAP) provided a detailed measurement of the anisotropies in the CMB [17]. This work was awarded by the Nobel Prize in Physics in 2006. Finally, ESA's Planck Space Telescope published the results which includes the highest resolution CMB map. Planck's findings support the inflationary theory, and also constrains the energy content of the Universe; 4.9% atoms, 26.8% dark matter and 68.3% dark energy. Planck also estimated the age of the Universe as 13.82 billion years [6]. The power spectrum of the CMB radiation temperature anisotropy, which can be seen in Figure 2.3 also contains physical signatures. The angular scale of the first acoustic peak determines the curvature of the Universe, the second one determines the reduced baryon density, and the third peak determines the dark matter density. The main information about the relation between the dark matter and the CMB radiation is that baryonic matter interacts with radiation whereas, dark matter does not. While, both affect the oscillations by their gravity, thus two forms of matter will have different effects. Therefore, measurements of the CMB radiation in the Universe provide perhaps the most compelling evidences that the dark matter is non-baryonic and the most precise measurements of its abundance.

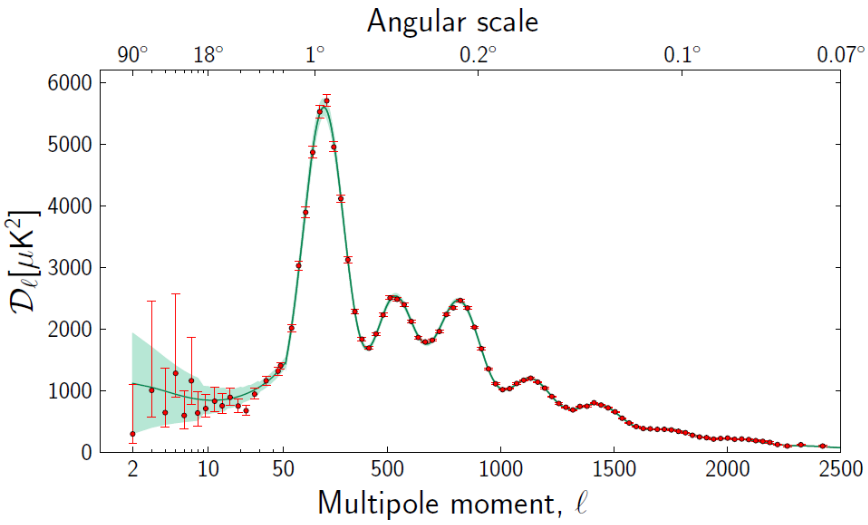

Figure 2.3: The power spectrum of the CMB radiation temperature anisotropy in angular scale, covering multipole moments l between 2 and 2500. The first, the second, and the third acoustic peaks give physical information about curvature of the Universe, reduced baryon density, and dark matter density, respectively [7].

After 2006, cold dark matter theory is favored by most cosmologists as a description of how the Universe went from small structures at early times (as shown by the CMB) to the bigger structures like galaxy clusters [13].

2.2 Particle Nature of Dark Matter

The leading dark matter particle candidates are assumed to be non-baryonic and cold, i.e., nonrelativistic. The strongest candidates are axions and weakly interacting massive particles (WIMPs). The axion is postulated as a possible solution to strong CP problem in QCD [42]. The axion mass is constrained to be near 10^{-5} eV [34]. WIMPs are stable particles which can arise in several extensions of the Standard Model such as supersymmetry and hidden valley theories, and are the main concern of this section.

Supersymmetry (SUSY) is a beyond SM theory which relates bosons and fermions. In SUSY, each SM fermion have a boson superpartner, and vice versa. The most discussed and theoretically developed WIMP candidate is the neutralino, the lighest supersymmetric particle (LSP) in many SUSY theories. R-parity, which is an exact discrete symmetry, predicts that the LSP is stable. Neutralino is a linear combination of the supersymmetric particles photino, higssino, and Z-ino which are the superpartners of photon, Higgs, and Z, respectively. It is predicted by SUSY that the neutralino has a mass less than a few TeV and interacts weakly with ordinary matter. If a WIMP like neutralino exists, it should have a cosmological abundance $\Omega \sim 1$, and can account for dark matter in the Universe today [34].

If WIMPs are responsible for the flatness of galactic rotation curves, then the local halo density should be around $0.3\ GeV cm^{-3}$, and they should have a Maxwell-Boltzmann distribution with a velocity dispersion of about $220\ km\ s^{-1}$ [34]. WIMPs should have a non-zero coupling to ordinary matter, as they must annihilate in the early Universe.

2.3 Detecting Dark Matter

If dark matter has a particle nature, and if it interacts with matter, it must do so through three mechanisms. These are the annihilation, the production, and the scattering. Each mechanism requires different experiments for detection, and a combination of these are required for discovery. The indirect detection experiments search for the resultant particles from annihilation. The production of dark matter particles can only be tested in an accelerator such as at the LHC. Direct detection experiments are sensitive to the scattering channel. The direct detection and the indirect detection experiments, and the accelerator searches will be mentioned in this section.

2.3.1 Direct Detection

The dominant interaction mechanism is elastic scattering because of the low velocity of the WIMPs. These interactions are spin-independent. The differential recoil energy spectrum of this type of interaction is given by the formula [46]:

$$\frac{dR}{dQ} = \frac{\sigma_0 \rho_0}{\sqrt{\pi} v_0 m_\chi {m_r}^2} F^2(Q) T(Q) \tag{2.1}$$

where m_χ is the WIMP mass, ρ_0 is the WIMP density in the galactic halo, σ_0 is the scattering cross section between the WIMP and the nucleus, m_r is the WIMP-nucleus reduced mass which is $m_r = \frac{m_\chi m_N}{m_\chi + m_N}$, m_N is the mass of the nucleus, $F^2(Q)$ is the nuclear form factor, and finally $T(Q)$ is a dimensionless integral over the local WIMP velocity distribution.

In order to reduce the cosmic ray background, direct detection experiments mostly operate in deep underground laboratories. Two types of detector technologies are commonly used by direct detection experiments: cryogenic detectors and noble liquid detectors. Cryogenic detectors operate at temperatures below ~$100\ mK$ to detect the heat produced when a particle hits an atom in a crystal absorber, e.g., germanium. The work principle of noble liquid detectors depends on detecting the flash of the scintillation light produced by a particle collision in the noble liquid, e.g., xenon, argon.

XENON100 is a direct detection experiment operated at the Gran Sasso National Laboratory (LNGS) for 13 months. It uses liquid xenon for both target (ionization) and detection (scintillation signals). XENON100 set the best limit on WIMP-nucleon scattering cross section for WIMP masses above $8\ GeV/c^2$, with a minimum of $2 \times 10^{-45} cm^2$ at $55\ GeV/c^2$ which can be seen in Figure 2.4 [11].

The CAST experiment searches for axions. If axions exist, they can be detected by the conversion to photons in a strong magnetic field. The CAST uses an LHC magnet for that purpose. CAST analysis up to 2003 implied an upper limit to the axion-photon coupling of $g_{a\gamma} < 1.16 \times 10^{-10}\ GeV^{-1}$ at 95% CL for $m_a < 0.02\ eV$ [16].

2.3.2 Accelerator Searches

The main signature of dark matter particle produced at accelerator searches such as the LHC is missing transverse energy (MET) in the detector along with the other SM particles. Searches generally rule out certain parameters of phase space dependent on the model and free variables used. The latest results from ATLAS [2] and CMS [35]

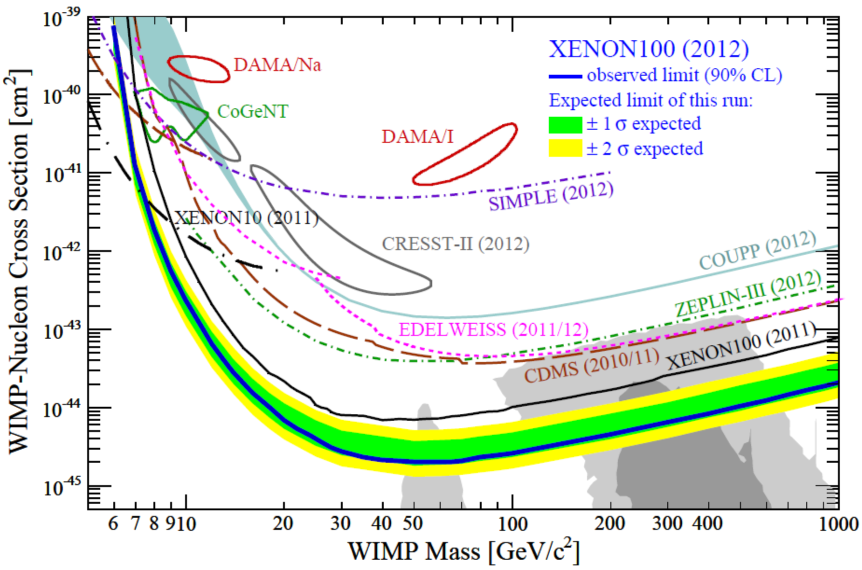

Figure 2.4: WIMP-nucleon spin-independent cross section limits from different direct detection experiments (color), and some theoretical predictions (grey) [11].

on dark matter searches mainly concentrate on different SUSY models while there are also searches for extra dimensions [37] and hidden valley [50] models.

Current searches are sensitive up to neutralino masses of about $1\ TeV$, and some SUSY models predicting masses up to $700\ GeV$ have been ruled out [1].

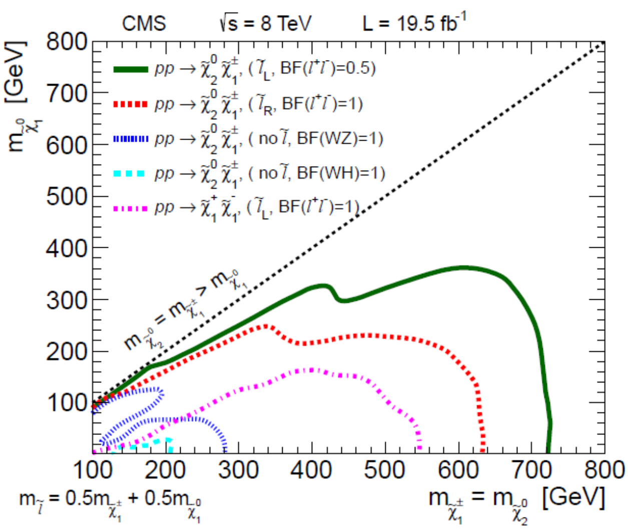

Figure 2.5: Exluded mass regions at 95% CL for chargino-neutralino production measured by CMS [35].

2.3.3 Indirect Detection

Particles are produced by the interaction of cosmic rays and interstellar medium, and it is called secondary production. Apart from secondary production, particles can also be created by dark matter particle annihilations. Collisions of dark matter in the galactic halo can annihilate into particle-antiparticle pairs such as ZZ, W^-W^+, HH, $\tau^-\tau^+$, $t\bar{t}$ etc. with kinematic constraints. However, these particles eventually decay into the handful stable particles of the SM, which are: e^-e^+, $p\bar{p}$, γ, and νs.

$$\begin{aligned}\chi + \chi &\to \bar{p} + ... \\ &\to e^+ + ... \\ &\to \gamma + ...\end{aligned}$$

While e^- and p are abundant in cosmic rays, a deviation from the expected smooth power law spectrum (due to Fermi acceleration and collision of particles) for $\bar{p}$, e^+, γ can indicate a dark matter signal. νs are notoriously hard to detect. ICECUBE experiment has an upper limit on the cross section as a function of WIMP mass from $300\ GeV$ to $100\ TeV$ for the annihilation into $\nu\bar{\nu}$ [3].

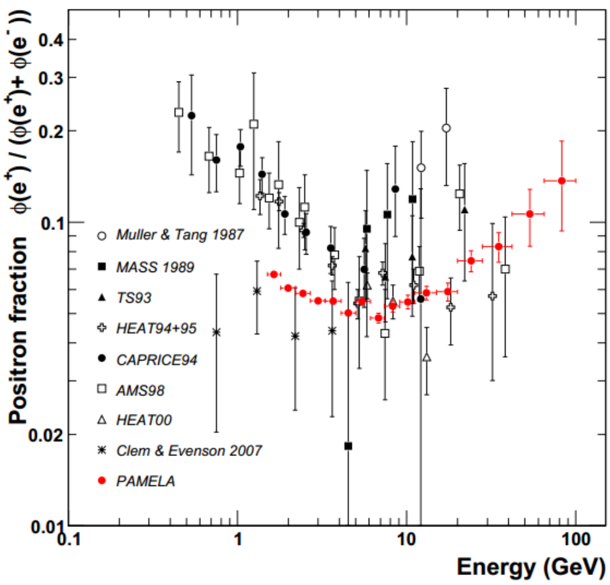

Figure 2.6: Positron fraction measured by PAMELA (red) compared with previous experiments (black) [8].

Figure 2.6 shows the positron fraction measured by PAMELA up to $100\ GeV$ compared with previous balloon experiments: Muller & Tang 1987 [39], Clem & Even-

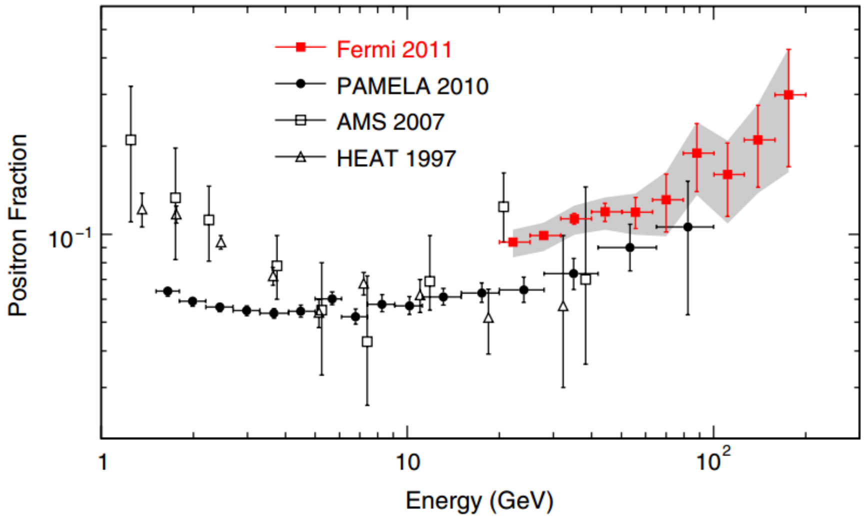

Figure 2.7: Fermi LAT positron fraction measurement (red) compared with other experiments [5].

son [27], HEAT94+95 [12], CAPRICE94 [20], HEAT00 [14], and a space experiment AMS-01 [9]. PAMELA had a total acquisition time of 500 days, and 151,672 electrons and 9,430 positrons were identified [8].

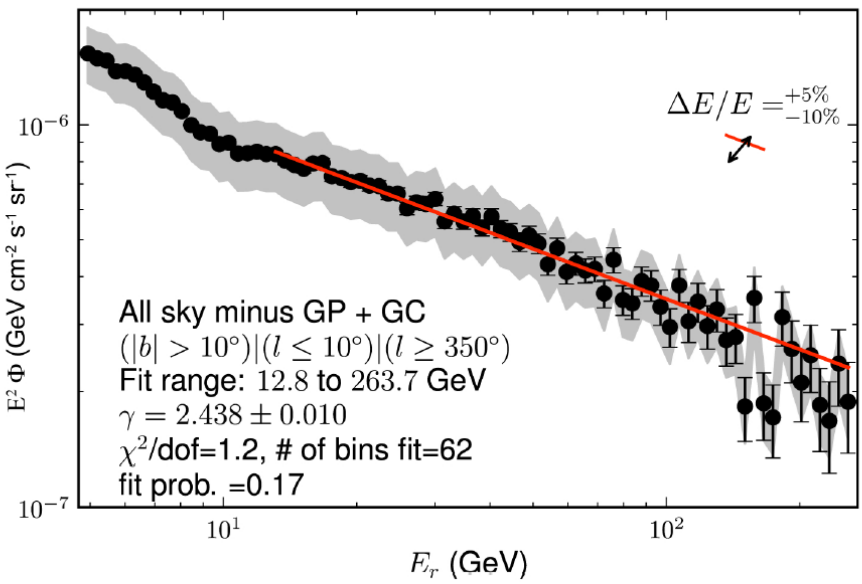

Figure 2.8: $E^2 \times \Phi$ versus energy, and a power law fit (red) by Fermi LAT. The grey band stands for systematic uncertainty [4].

Figure 2.7 shows the positron fraction measurement by Fermi LAT between 20 GeV and 200 GeV compared with previous results. While both PAMELA and Fermi data indicate a rise in the positron fraction above 30 GeV, the measurements are low in statistics and not in agreement with each other. More statistics and better energy resolution are required for a dark matter signature. Moreover, such an observation can point to possible production of positrons from nearby astrophysical sources, such as pulsars [23]. For a conclusive dark matter signature, the point where the spectrum falls must be observed, which requires higher energy measurement. AMS-02 which has a magnet, larger acceptance, and more acquisition time, measured the positron fraction with unprecedented accuracy, and it will be discussed in Chapter 3 in detail.

Figure 2.8 shows photon flux measured by Fermi LAT up to $263.7\ GeV$ and a power law fit [4]. There is also a suggestion that there might be a dark matter annihilation into two photons would give a sharp feature at the χ_0 mass [30].

2.4 Electron-Positron Pair Production

Since this analysis is based on converted photons, i.e. photons which make electron-positron pair production, it is necessary to briefly discuss pair production in this section.

The photon interaction with matter can be categorized according to: the type of target, e.g., electrons, nuclei, etc., and the type of event, e.g., absorption, scattering, electron-positron pair production, etc. The cross sections of a photon with Cu is shown in Figure 2.9 as an example. It can be seen in this figure that the dominant interaction after $10\ MeV$ is pair production.

Electron-positron pair production is one of the main processes that take place when the high energy photons interact with a nucleus. It occurs especially when there is an intensive flux of high energy γ rays [38]. If the photon energy $\hbar\omega$ is greater than $2m_ec^2$ near a nuclear Coulomb field, the photon can transform into an electron-positron pair.

The reaction for pair production is denoted by $\gamma + M \ \rightarrow \ M + m_e + m_e + Q$, and the threshold condition for the process is given as

$$T_{th} = 2m_ec^2 = 1.022\ MeV \tag{2.2}$$

If we consider the positron as a hole in the sea of negative electrons, its energy and

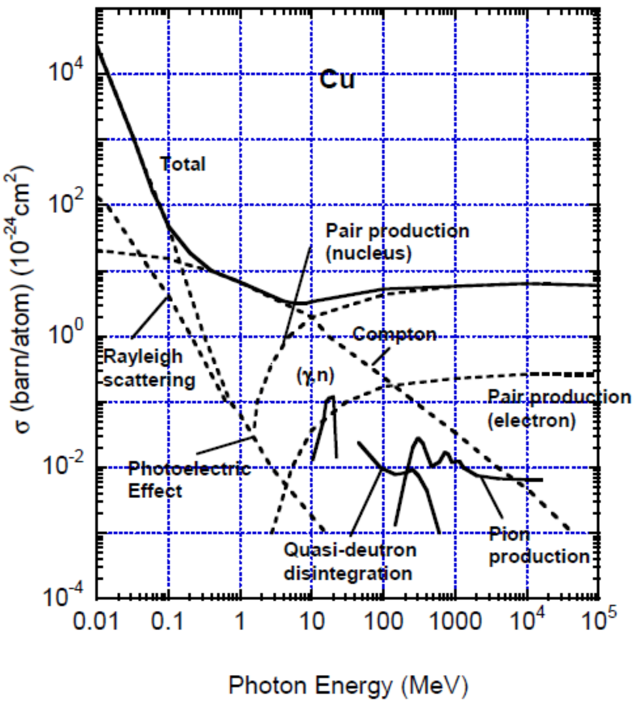

Figure 2.9: Photon cross section for Cu in the energy range between 10 keV and 100 GeV [33].

momentum can be given as $E_+ = -E$ and $\vec{p}_+ = -\vec{p}$. The energy of the electron is denoted by $E_0 = E$, hence the energy of the positron is $E_+ = |E|$. At the end of the process, it can be observed that the photon is absorbed and an electron-positron pair occur with energies E_0 and E_+, respectively. Also, θ_+ is the angle between the direction of motion of positron and the direction of incident photon, and ϕ_+ is the azimuthal angle between them.

The differential cross section for the process [19] is given as

$$\begin{aligned} d\phi &= -\frac{Z^2}{137}\frac{e^4}{2\pi}\frac{p_0p_+}{k^3}dE_0\frac{sin\theta_0 d\theta_0 sin\theta_+ d\theta_+ d\phi_+}{q^4}\left\{\frac{p_+^2 sin^2\theta_+(4E_0^2-q^2)}{(E_+-p_+cos\theta_+)^2}\right. \\ &+ \frac{p_0^2 sin^2\theta_0(4E_+^2-q^2)}{(E_0-p_0cos\theta_0)^2} + \frac{2p_0 2p_+ sin\theta_0 sin\theta_+ cos\phi_+(4E_0E_+ + q^2)}{(E_0-p_0cos\theta_0)(E_+-p_+cos\theta_+)} \\ &- \left.\frac{2k^2(p_+^2 sin^2\theta_+ + p_0^2 sin^2\theta_0 + 2p_0p_+ + sin\theta_0 sin\theta_+ cos\phi_+)}{(E_0-p_0cos\theta_0)(E_+-p_+cos\theta_+)}\right\} \end{aligned} \quad (2.3)$$

Thus, the integration over the angles yields to the cross section for the electron-positron pair production with energies E_0 and E_+ as follows,

$$\begin{aligned}
\phi(E_0)dE_0 &= \frac{Z^2}{137}\left(\frac{e^2}{m_ec^2}\right)^2\frac{p_0p_+}{k^3}dE_0\Big\{-\frac{4}{3}-2E_0E_+\frac{p_0^2+p_+^2}{p_0^2p_+^2} \\
&+ \mu^2\left(\frac{\epsilon_0E_+}{p_0^3}+\frac{\epsilon_+E_0}{p_+^3}-\frac{\epsilon_+\epsilon_0}{p_0p_+}\right)+\left[\frac{k^2}{p_0^3p_+^3}(E_0^2E_+^2+p_0^2p_+^2)-\frac{8}{3}\frac{E_0E_+}{p_0p_+}\right]log \\
&+ \frac{\mu^2k}{2p_0p_+}\left[\frac{E_0E_+-p_0^2}{p_0^3}\epsilon_0+\frac{E_0E_+-p_+^2}{p_+^3}\epsilon_++\frac{2kE_0E_+}{p_0^2p_+^2}\right]log\Big\} \qquad (2.4)
\end{aligned}$$

where

$$\begin{aligned}
\epsilon_+ &= 2log\frac{E_++p_+}{\mu} \\
log &= log\frac{E_0k-p_0^2+p_0p_+}{E_0k-p_0^2-p_0p_+}=2log\frac{E_0E_++p_0p_++\mu^2}{\mu k}
\end{aligned} \qquad (2.5)$$

It can be observed that this cross section formula is symmetrical in E_0 and E_+ [19]. The energy conservation results in $\hbar\omega = E_0 + E_+$.

The total cross section can be obtained by integrating over all possible values of electron energy E_0. The integration offers analytical solutions for two cases; the intermediate photon energy limit and the ultrarelativistic limit [38].

If there is no screening and the photon energy is in the intermediate range, $1 \ll \hbar\omega/m_ec^2 \ll 1/\alpha Z^{1/3}$, the cross section for photons can be written as

$$\sigma_{pair} = \alpha r_e^2Z^2\left[\frac{28}{9}ln\left(\frac{2\hbar\omega}{m_ec^2}\right)-\frac{218}{27}\right]m^2atom^{-1} \qquad (2.6)$$

where r_e is the classical electron radius and $\alpha = 1/137$ is the fine structure constant. The probability of pair production increases with increasing photon energy. Born approximation is used to approximate the cross section without the screening effect.

In the case of complete screening and in the ultra relativistic limit of the photon energies $\hbar\omega/m_ec^2 \gg 1/\alpha Z^{1/3}$, the cross section becomes

$$\sigma_{pair} = \alpha r_e^2Z^2\left[\frac{28}{9}ln\left(\frac{183}{Z^{1/3}}\right)-\frac{2}{27}\right]m^2atom^{-1} \qquad (2.7)$$

For the purpose of this thesis, it must be noted that the cross section is nearly constant with increasing energy in this region.

Table 2.1 shows the cross section values for C and Al from $10\ MeV$ to $100\ GeV$. It can be seen from both Figure 2.9 and Table 2.1 that cross section values become almost constant after $10\ GeV$.

Table 2.1: The cross section values for two nucleus, Z = 6 Carbon and Z = 13 Aluminum.

σ_{pair} $[barn^2 atom^{-1}]$ / Photon Energy $h\nu$	Carbon Z = 6	Aluminum Z = 13
10 MeV	0.07686	0.3584
100 MeV	0.2079	0.9503
1 GeV	0.2805	1.237
10 GeV	0.2975	1.300
100 GeV	0.3002	1.309

Table 2.2: The angle between the incident photon and emerging electron (or positron).

Photon Energy ($h\nu$)	θ $[degrees]$
10 MeV	2.9278
100 MeV	0.2927
1 GeV	0.0292
10 GeV	0.0029
100 GeV	0.0002

The average angle between the incident photon and the emitted electron (or positron) can be given as

$$\theta = \frac{m_e c^2}{h\nu} \qquad [rad] \tag{2.8}$$

Table 2.2 shows the angle between the incident γ and produced electron (or positron) between energies of 10 MeV and 100 GeV. It should be noted that θ is so small after 10 GeV that the resultant e^+e^- pair continues their path together which is important for this thesis.

The mean free path for a gamma ray to travel in a material before the pair production occurs is defined as λ_{pair} and related with the total cross section by the relation $\frac{1}{\lambda_{pair}} = N\sigma_{pair}$, where N denotes the atom density in the material. In the case of total screening, the pair production can occur in the field of an atomic electron and the total cross section can simply be evaluated by substituting $Z(Z+1)$ instead of the Z^2 term in Equation 2.7. Hence, the mean free path for a gamma ray in the ultrarelativistic limit can be written as follows,

$$\frac{1}{\lambda_{pair}} = N\sigma_{pair} = \frac{7}{9}4Z(Z+1)Nr_e^2\alpha ln\left(\frac{183}{Z^{1/3}}\right) \tag{2.9}$$

where the small constant term in Equation 2.7 can be ignored. The mean free path can also be related with the target radiation length, χ_0, as

$$\lambda_{pair} = \frac{9}{7}\chi_0 \tag{2.10}$$

where χ_0 is the radiation length of the material, usually measured in $g\ cm^{-2}$. χ_0 is the mean distance for an electron loses all but $1/e$ of its energy, and $7/9$ of the mean free path for pair production by a photon. The ECAL in the AMS-02 has $17\ \chi_0$ in total.

CHAPTER 3

AMS-02 DETECTOR

First, the AMS-02 subdetectors will be outlined in this chapter. Photon analyses can be done in two ways with the AMS-02. These methods will be explained. Finally, the latest AMS-02 results will be briefly discussed.

3.1 Overview

The AMS-02 is the first large magnetic spectrometer in the space. To measure the cosmic particles with an unprecedented accuracy, it has seven subsystems which is shown in Figure 3.1:

- Magnet bends particles and antiparticles in opposite directions.
- Transition Radiation Detector (TRD) identifies electrons and positrons among other particles.
- Time of Flight System (ToF) provides fast trigger and measures particle velocity.
- Silicon Tracker determines charge sign of the particles.
- Ring Imaging Čerenkov Detector (RICH) measures the velocity of the particle.
- Anticoincidence Counters (ACC) veto particles passing through the magnet.
- Electromagnetic Calorimeter (ECAL) measures the energy of electrons, positrons, and photons, i.e., electromagnetically interacting particles.

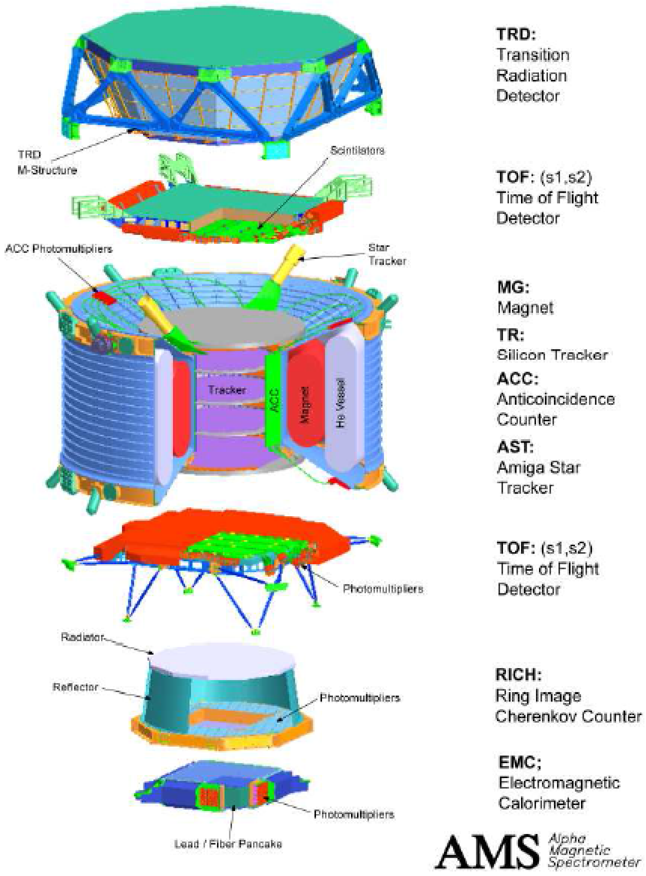

Figure 3.1: An exploded view of AMS-02 [31].

In AMS-02 $\hat{z} = -1$ defines a downward going particle. The magnetic field points along the x-direction in the AMS coordinate system. Therefore, yz plane is the bending plane.

3.2 Subdetectors

3.2.1 Magnet

Particles and their antiparticle counterparts have almost the same properties; for instance, they have the mass, but they have opposite charges. Particles and antiparticles can be separated simply by using a magnetic field. In a uniform magnetic field, particles and antiparticles are bent in opposite directions.

The AMS-02 magnet consists of Neodymium-Iron-Boron sectors. The magnet has a peak magnetic flux of $0.15\ Tm^2$, and an acceptance of $0.82\ m^2 sr$. The configuration has a negligible dipole moment outside the magnet. It is required not to have an undesirable force on the ISS [49].

3.2.2 Transition Radiation Detector (TRD)

When charged particles cross the boundary between two media which have different dielectric constants, they emit transition radiation. Although the probability of a particle to emit transition radiation at a single interface is about 10^{-2}, this can be increased by adding several layers. The TRD of AMS-02 is formed of 20 layers, the edges of which can be seen in Figure 3.2. Each layer consists of $20\ mm$ of thick fleece used as radiator and straw tubes which have $6\ mm$ diameter and filled with Xe-CO_2 gas mixture used as detector [31].

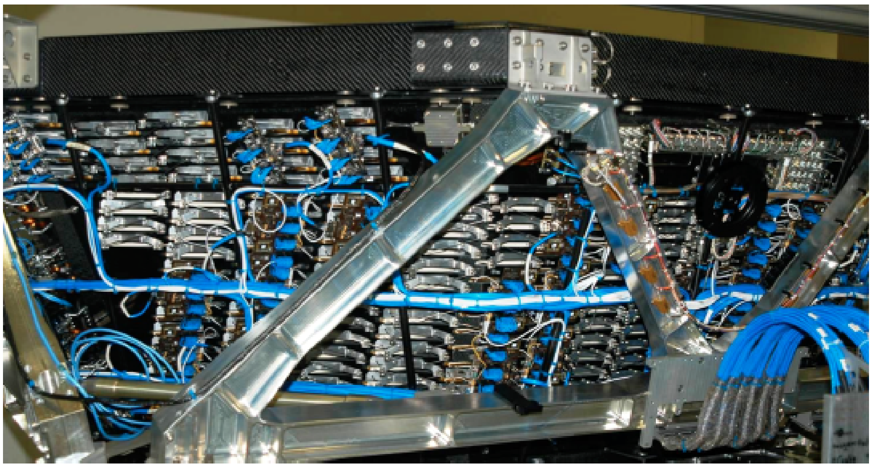

Figure 3.2: The Transition Radiation Detector (TRD) seen from the side, readout elements, and support structure [49].

Both the primary particle and the emitted X-ray photon ionize the gas mixture in the straw tubes. The ionized gas starts an ionization avalanche in the vicinity of a thin wire at high voltage. This abrupt current change induces a fast electric signal. The X-ray contribution to the ionization signal adds up with the ionization signal of a charged particle traversing the gas. The intensity of the transition radiation is proportional to the Lorentz factor

$$\gamma = \frac{E}{m_0 c^2} \tag{3.1}$$

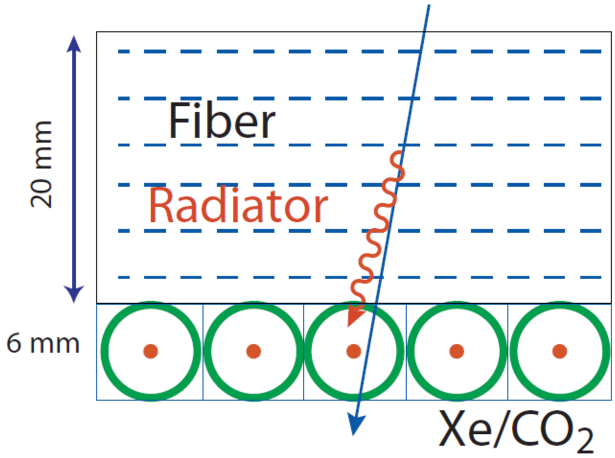

Figure 3.3: The working principle of AMS-02 TRD. Incoming particle is in blue, the TR photon is in red, and the straw tubes which are filled with Xe-CO_2 gas mixture are in green [49].

where E is the energy, m_0 is the rest mass of the particle, and c is the speed of light. Hence, electrons are more likely to have this transition radiation contribution to ionization than more massive particles like protons at the same energy.

Figure 3.3 shows the working principle of the TRD. Incoming particle (blue) emits TR (red), and both the particle and the TR ionizes the gas mixture in the straw tube (green).

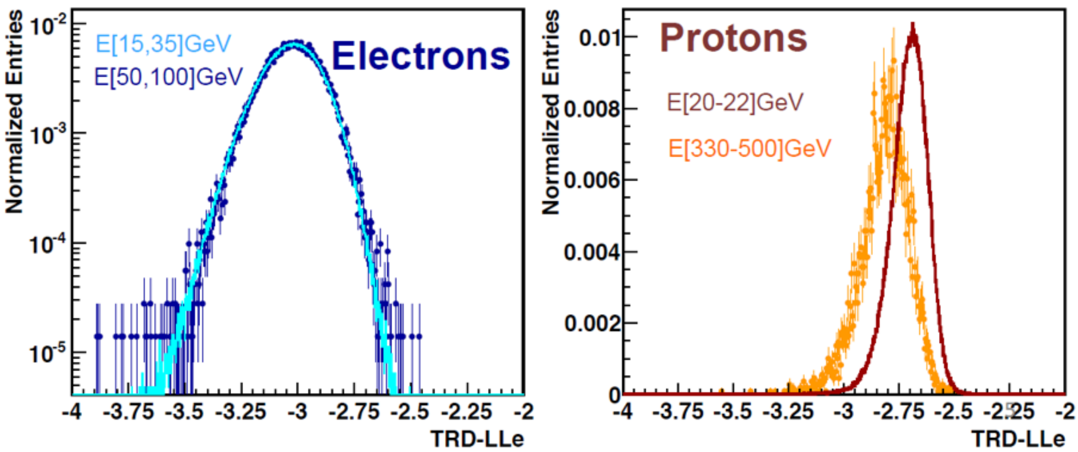

Figure 3.4: TRD-LLe distribution for electrons with energies between 15 and 35 GeV, and 50 and 100 GeV (left), and for protons with energies between 20 and 22 GeV, and 330 GeV (right) [46].

In order to separate electrons and protons, a log-likelihood method is developed using signals from all the TRD layers. Figure 3.4 shows the difference of log-likelihood probability of the electron hypothesis (TRD-LLe) between an electron and proton sample [46]. It can be seen in the figure that electrons have almost no shift with different energies. However, protons have a shift towards electron like values with increasing energy because the Lorentz factor γ becomes appreciable.

3.2.3 Silicon Tracker

The silicon tracker is composed of double-sided silicon microstrip sensors, each has an active volume of $41.360 \times 72.045 \times 0.300\ mm^3$ [24]. The silicon sensors are grouped together for readout and biasing in ladders. Nine planes are then formed by these ladders. One of the nine planes is shown in Figure 3.5. The spatial resolution is 10 μm in the bending plane (yz), and 30 μm in the non-bending plane (xz).

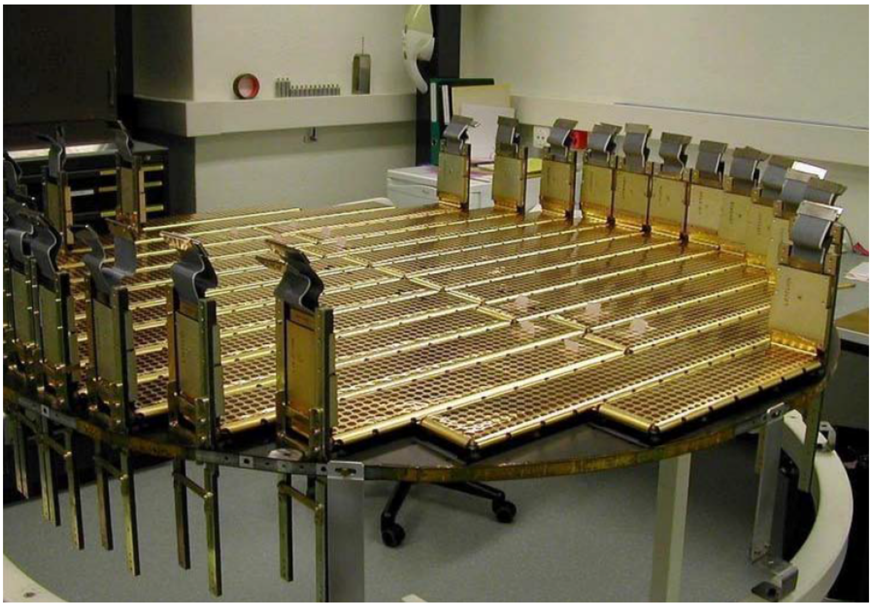

Figure 3.5: One of the nine tracker planes which consists ladders that are made of double sided silicon microstrip sensors [49].

When a charged particle passes through a ladder, the electron-hole pairs are produced. The analogue signal is generated by the acceleration of electrons under a bias voltage. The signal is then integrated and digitized. The exact position of the hit is determined by fitting the signal cluster. The tracker hits are combined to reconstruct the track of the particle. The best-fit curve and the rigidity of the particle are determined by minimizing the residuals δ_x and δ_y.

AMS-02 as a space instrument have to deal with two main problems: the vibrations during the transport before deployment and periodic temperature fluctuations due to solar radiation and cooling because of the shadow of the Earth. In order to have reliable data from the Tracker under these effects, AMS-02 has a laser alignment system. This system generates optical signals which imitate straight particle tracks, and traces the movement in the tracker geometry with an accuracy of $5\mu m$ [49].

3.2.4 Anticoincidence Counters (ACC)

The Anticoincidence Counters are a layer of scintillators which surround the Silicon Tracker. The ACC is formed by 16 scintillation panels of $8\ mm$ thickness. The particles entering the tracker laterally, i.e., outside of the main acceptance, can be detected by the ACC, then undesired particles can be vetoed in the trigger system [49].

Figure 3.6 shows how the ACC works. Events which pass through the magnet are rejected. Secondary particles coming from the interaction of the incident particle in the AMS-02 can be identified, and are not rejected by the ACC.

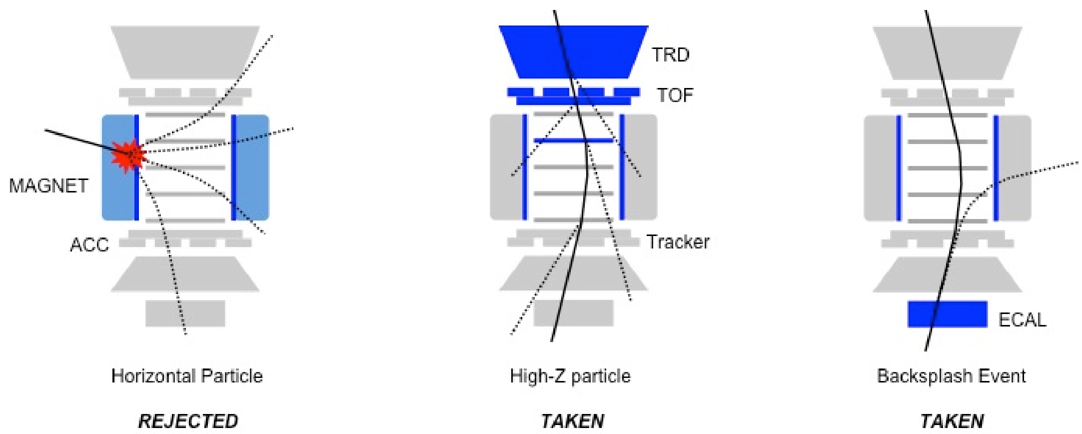

Figure 3.6: Working principle of the ACC. Incident particles which hit the magnet are rejected [48].

3.2.5 Time of Flight (TOF)

The Time of Flight is a scintillator system which has four planes grouped as two pairs shown in Figure 3.7, positioned below and above the magnet. The active area of each plane is $1.2m^2$ [49]. The paddles are overlapped by $0.5\ cm$ in each plane to avoid geometrical inefficiencies. The paddles in a pair of planes are perpendicular to each other for efficient background rejection. The ToF provides fast trigger for charged particles and converted photons, measures particle velocity, and discriminates upward and downward going particles. The time resolution of the ToF system is $120\ ps$. The ToF can also measure the absolute charge of the particle. The geometrical acceptance of the system is $0.4\ m^2sr$ [49].

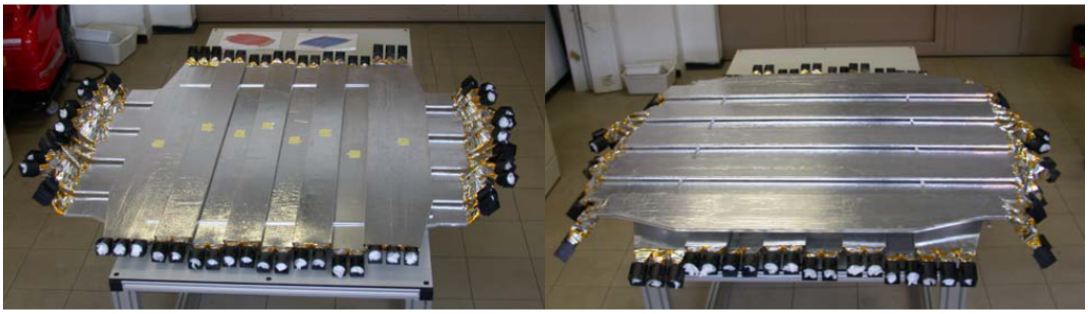

Figure 3.7: The upper (left) and the lower (right) ToF planes during assembly [49].

Figure 3.8 shows the absolute charge measurement in the upper ToF by the combination of measurements from two layers of scintillating counters [41].

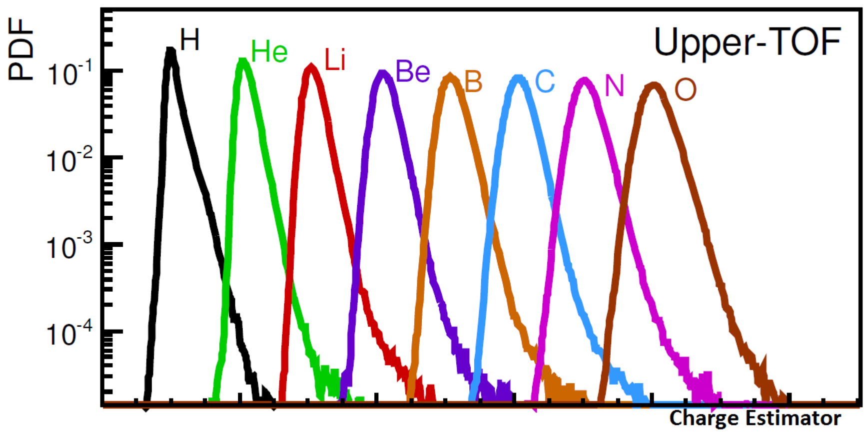

Figure 3.8: Particle charge magnitude evaluated by the upper ToF. Lower ToF is also gives similar results with upper ToF [41].

3.2.6 Ring Imaging Čerenkov Detector (RICH)

For an analysis such as the search of antimatter or relative abundances of isotopes, the mass measurement is essential. The mass is related to the momentum and the velocity of the particle by the formula

$$m = \frac{p}{\beta c}\sqrt{1-\beta^2} \tag{3.2}$$

where m is the mass, p is the momentum of the particle, c is the speed of light in a vacuum, and β is the ratio of the velocity of the particle to the speed of light. Thus, these two quantities (p and β) must be measured. The momentum information is obtained from the Silicon Tracker with a relative accuracy of 1% over a wide range of energies. This error appears also on the mass of the particle, so the velocity has to be measured with a relative accuracy of about 1 per mil [49]. Ring Imaging Čerenkov Detector serves this purpose. Figure 3.9 shows the parts of the RICH: the silica aerogel radiator, the mirror, and the photomultipliers.

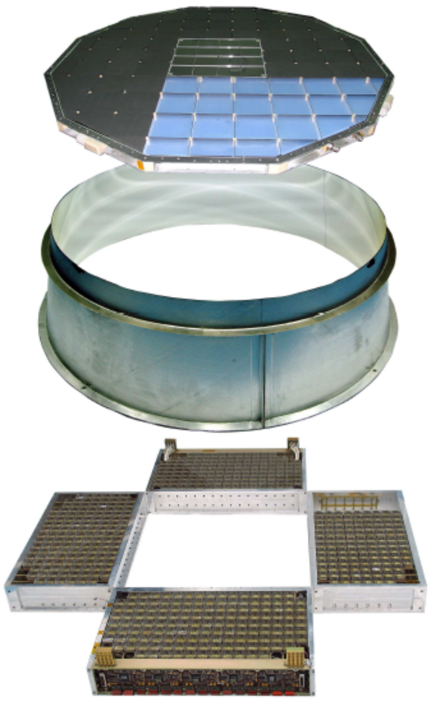

Figure 3.9: Exploded view of the RICH. The radiators plane (top), the conical reflecting mirror (middle), and the detection plane (bottom) [40].

The velocity can be measured using the Čerenkov effect. The Čerenkov radiation consists of photons emitted along a characteristic cone whose angular aperture is directly related to the particle velocity and with the index of refraction of the material. The Čerenkov angle is related with β given by the formula

$$\theta_C = \frac{1}{n\beta} \tag{3.3}$$

where θ_C is the Čerenkov angle, n is the index of refraction of the material, and β is v/c. Then β measurement is directly related with the reconstruction of θ_C [22].

3.2.7 Electromagnetic Calorimeter (ECAL)

The Electromagnetic Calorimeter is a sampling calorimeter made of lead-scintillating fibers which can be seen in Figure 3.10. The active volume of the ECAL is $638\ kg$ and $68.5 \times 68.5 \times 16.7\ cm^3$. When a particle traverses the active volume, produced light is collected by 324 photomultipliers (PMTs). The ECAL measures the energy deposition, and attains 3-dimensional image of the longitudinal and lateral shower development. The ECAL has 18 superlayers, each of which has an $18.5\ mm$ thickness. Each layer is composed of 11 grooved, $1\ mm$ thick lead foils, and $1\ mm$ diameter scintillating fibers glued together. The ECAL has 17 χ_0 in total [43].

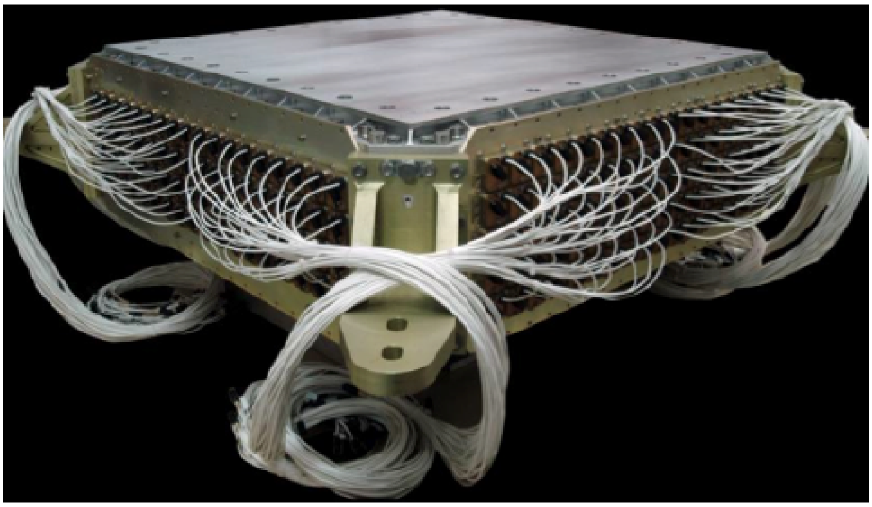

Figure 3.10: The Electromagnetic Calorimeter (ECAL). The fibers and the support structure can be seen [49].

An efficient way of separating positrons from protons is needed for both lepton and conversion mode photon analysis. The ECAL is a specialized detector which is able to distinguish positrons from protons and electrons from antiprotons with an identification power of one positron over 10^5 protons. When a high-energy electron, positron or photon passes through a material with a high Z, many other electrons, positrons and photons of lower energy are produced, i.e., electromagnetic shower. When a high energy proton passes through the material, it mostly behaves as a minimum ionizing particle (MIP). However, it produces several pions, kaons etc. if it interacts with the material, i.e., hadronic shower. Protons and positrons can be identified by investigating the ECAL shower profiles. The direction of the incident particle can also be determined from the shower shape.

3.3 AMS-02 as a Photon Detector

Depending on the interaction point of the photon in the detector, the photon analysis can be done in two ways: Calorimetric mode, and conversion mode, which will be discussed here.

3.3.1 Calorimetric Mode

The material density in the subdetectors of AMS-02 above the ECAL was designed to be at a minimum. This is required to minimize the effects of multiple scattering, and to ensure the confidence of the measured variables such as rigidity. This fact allows a photon to pass through the detector without interacting the material down to the ECAL. Such a photon is called a calorimetric photon. In Figure 3.11 a typical calorimetric Monte Carlo (MC) event is shown.

While more energetic events can be analyzed with this mode compared with the conversion mode, angular resolution of the events are limited by the angular resolution of the ECAL.

3.3.2 Conversion Mode

Although the material density of the subdetectors is low except the ECAL, there is still a probability for a photon to make an e^+e^- pair production. If the primary photon converts at or above the upper ToF plane, a pair of tracks can be found and a vertex

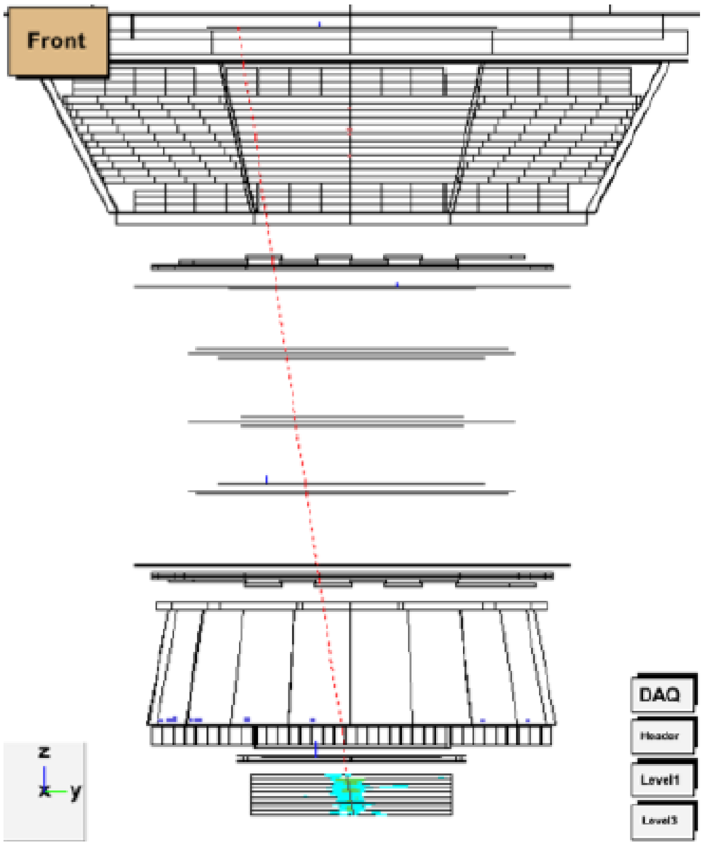

Figure 3.11: An AMS-02 event display shows a downward going MC photon showering in the ECAL. Few hits in the RICH and the Tracker are due to the backscattered particles. Red dashed line indicates the reconstructed photon direction, i.e., there is no track [30].

can be reconstructed. However, when photons above $50\ GeV$ convert, the Silicon Tracker cannot spatially resolve two tracks of e^+ and e^-. The two tracks seem as one particle track; therefore, a vertex cannot be found. However, up to $50\ GeV$ the angular resolution of the Tracker can be used which is far better than the angular resolution of the ECAL.

3.4 AMS-02 Results

The first AMS-02 paper, 'First Result from the Alpha Magnetic Spectrometer on the International Space Station: Precision Measurement of the Positron Fraction in Primary Cosmic Rays of $0.5-350\ GeV$' was published on Physical Review Letters on

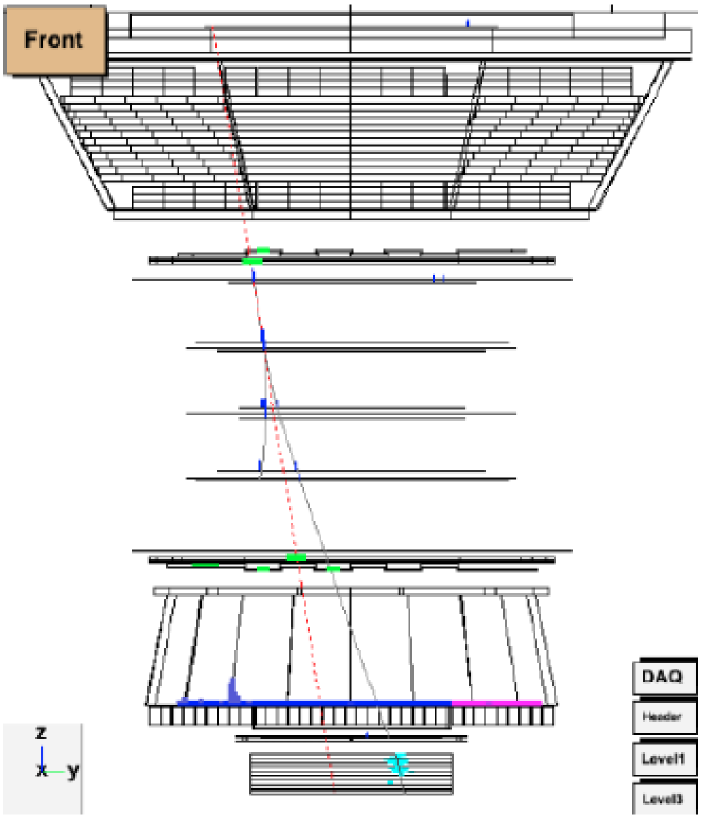

Figure 3.12: An AMS-02 event display shows an MC photon convert in the upper ToF, and the e^+e^- pair bend in opposite directions in the inner Tracker due to magnetic field. While the e^+ escapes the AMS-02 volume, the e^- gives a shower in the ECAL [30].

the 5th of April, 2013. The paper includes 18 months of collected data from 19 May 2011 to 10 December 2012, which is only approximately 8% of the expected AMS-02 data. The paper presents the ratio of the positron flux to the combined electron-positron flux between 0.5 to 350 GeV energy range. Approximately 25 billion events are analyzed.

The measured positron fraction as a function of reconstructed energy is shown in Figure 3.13. In the figure, up to 10 GeV, there is a decline with increasing energy because of the secondary production of particles. After 10 GeV, the steady increment points that there is another mechanism besides the secondary production of positrons. The behavior after 250 GeV can be understood with more statistics. There is no observed fine structure in the energy spectrum. An anisotropy study is conducted using

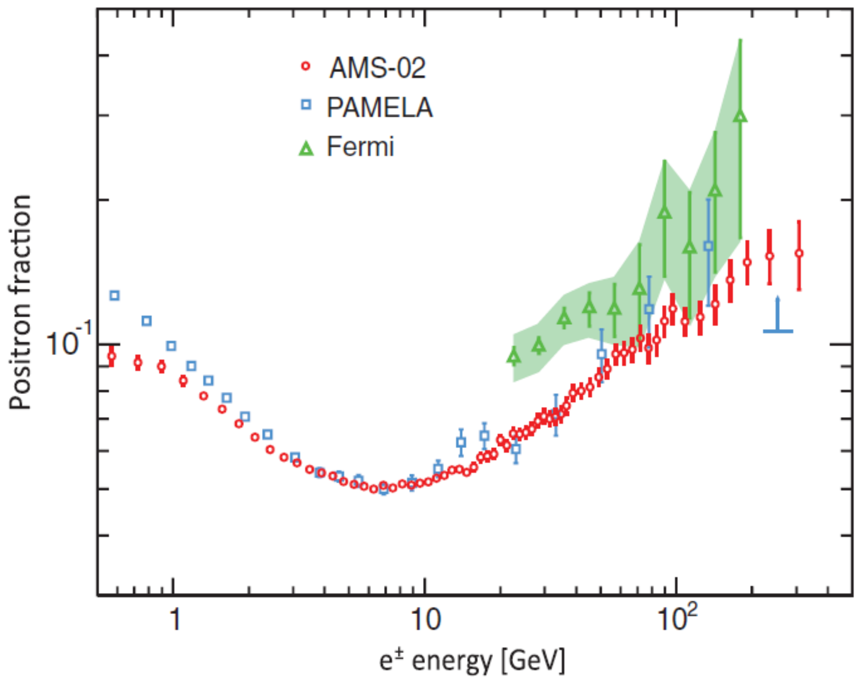

Figure 3.13: The AMS-02 positron fraction compared with PAMELA and Fermi-LAT [10].

the sample from 16 to 350 GeV, and the positron to electron ratio shows consistency with isotropy. These results points to a new physical phenomena which can have a particle physics or an astrophysical physics origin [10].

There are seven proceedings which were presented at 33rd International Cosmic Ray Conference, Rio De Janeiro 2013, The Astro-particle Physics Conference (ICRC 2013) which was held between 2 and 9 July 2013.

Precision measurement of the positron fraction in primary cosmic rays of 0.5-350 GeV

There is no fine structure in the positron fraction shown in Figure 3.14. From 20 to 250 GeV the slope decreases by an order of magnitude [36].

Determination of the positron anisotropy with AMS

The anisotropy study is conducted with $35,000$ positron events in the energy range of $16 - 250$ GeV. The positron to electron ratio at any angular scale seems to be isotropic. The upper limit on the dipole anisotropy parameter is set to 0.030 with a 95% confidence level [25].

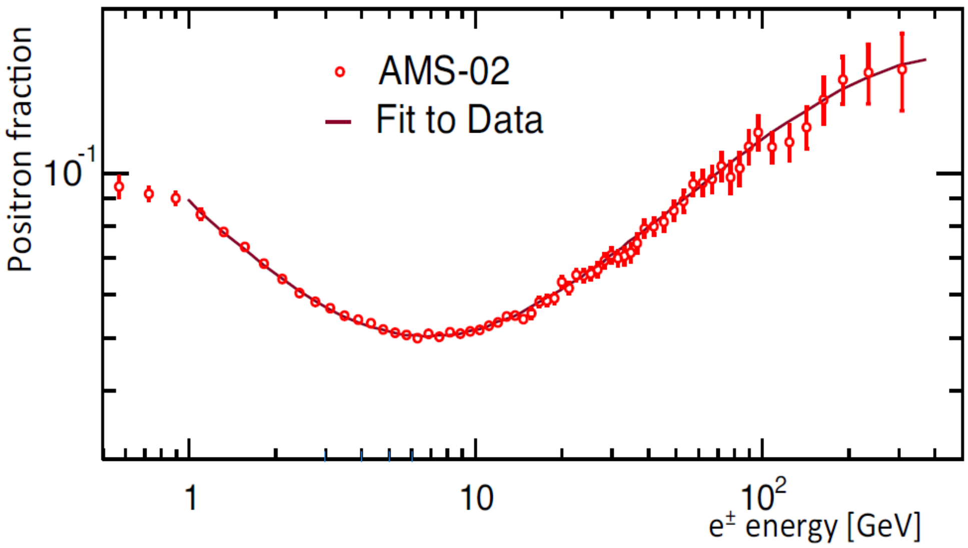

Figure 3.14: The positron fraction measured by AMS-02 and fit with the minimal model [36].

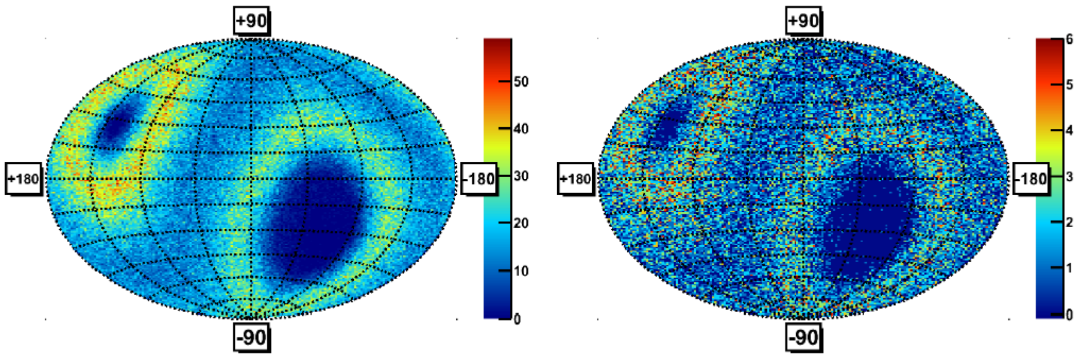

Figure 3.15: Galactic maps of the electron (left) and positron (right) events in the energy range of $16 - 350\ GeV$. The colors represent the number of events per bin [25].

Precision measurements of the electron spectrum and the positron spectrum with AMS

Measured fluxes multiplied by the third power of the energy are shown in Figure 3.16. This analysis consists of 10% of the total expected data. The largest energy bin of the electron flux measurement is $500\ GeV$. The multiplied electron flux is increasing up to $10\ GeV$, and it starts to decrease after $10\ GeV$. While, the result is in agreement with the previous experiments such as HEAT and PAMELA in their mid-range, the effect of solar modulation is significant at low energies. The AMS-02 measurement extends up to 350 GeV with the positron flux is increasing up to 10 GeV, going flat between $10 - 30$ GeV, and then increasing again. It is noteworthy that the spectral index and its energy dependence is different between the electron and the positron spectrum [47].

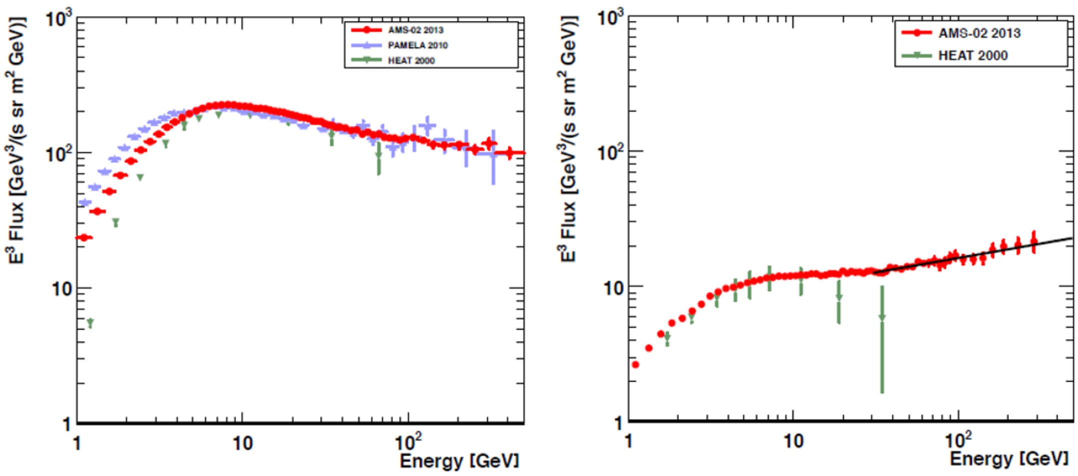

Figure 3.16: Measured electron (left) and positron (right) fluxes by AMS-02 compared with HEAT and PAMELA [47].

Precision measurement of the e^+ + e^- spectrum with AMS

Measured events are in the energy range between 0.5 and 700 GeV, which is shown in Figure 3.17. 10% of the total expected data are used. There is no fine structure in the spectrum unlike ATIC and PPB-BETS results. Nevertheless, there is a change in the spectral distribution which can be better observed in separate electron and positron flux measurements. This change can be compatible with the AMS-02 positron fraction result. Systematical error studies still continue [18].

Precision measurement of the proton flux with AMS

The measured proton flux multiplied by $E^{2.7}$ is shown in Figure 3.18. There is no fine structure in the spectrum. The high energy region is consistent with the single power law spectra. The flux below 30 GV is affected by the solar modulation [32].

Precision Measurement of the Cosmic Ray Helium Flux with AMS Experiment

The measured helium spectrum in the rigidity range from 2 GV to 3 TV is shown in

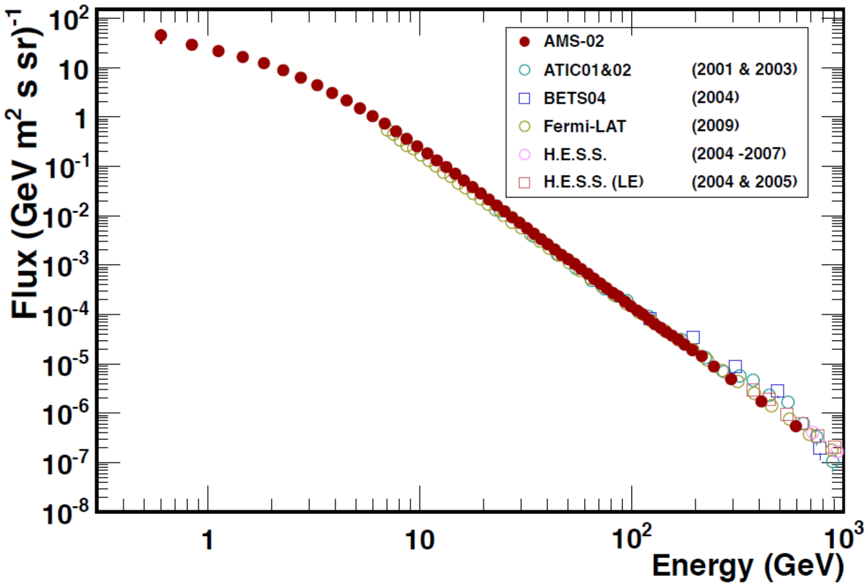

Figure 3.17: Combined electron – positron spectrum compared with previous experiments [18].

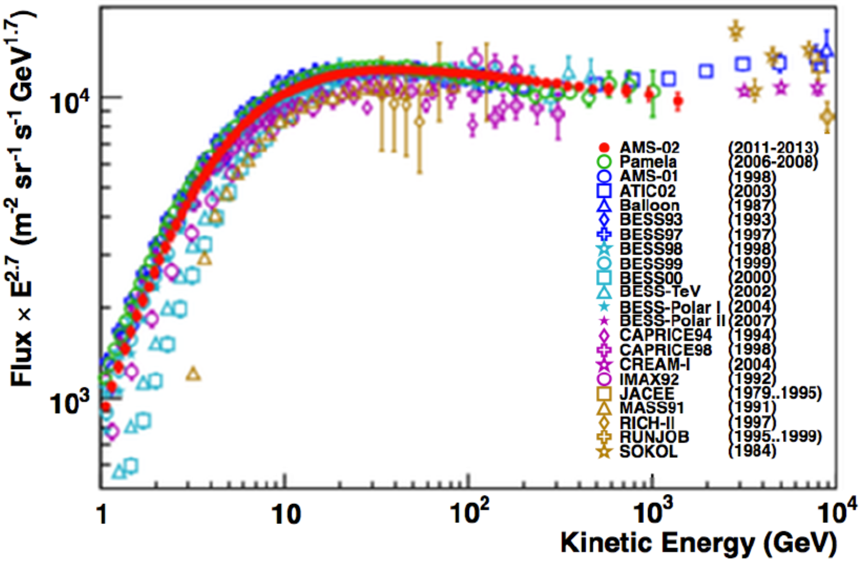

Figure 3.18: The average proton flux of AMS-02 compared with previous experiments [32].

Figure 3.19. The spectrum is modulated by the time dependent solar activity below $10\ GV$. The spectrum can be parametrized by a single power law spectrum. There is no fine structure [26].

Precision Measurement of the Cosmic Ray Boron-to-Carbon Ratio with AMS

AMS-02 can distinguish nuclei from $Z = 1$ to $Z = 26$ up to TeV/n. Boron to

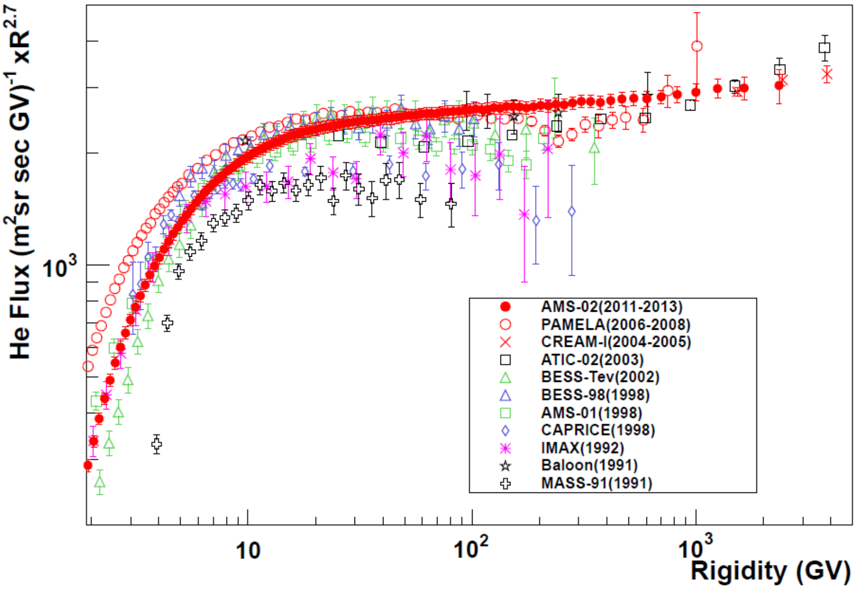

Figure 3.19: The measured helium spectrum multiplied by the rigidity value in the 2.7 power by AMS-02 compared with the previous experiments [26].

carbon ratio measurement is important because it is sensitive to propagation modeling of cosmic rays. The derived boron to carbon ratio in the energy range from 0.5 to $700\ GeV/n$ is shown in Figure 3.20. Statistics is the main limitation at high energies for the ratio measurement and the statistical error calculation [41].

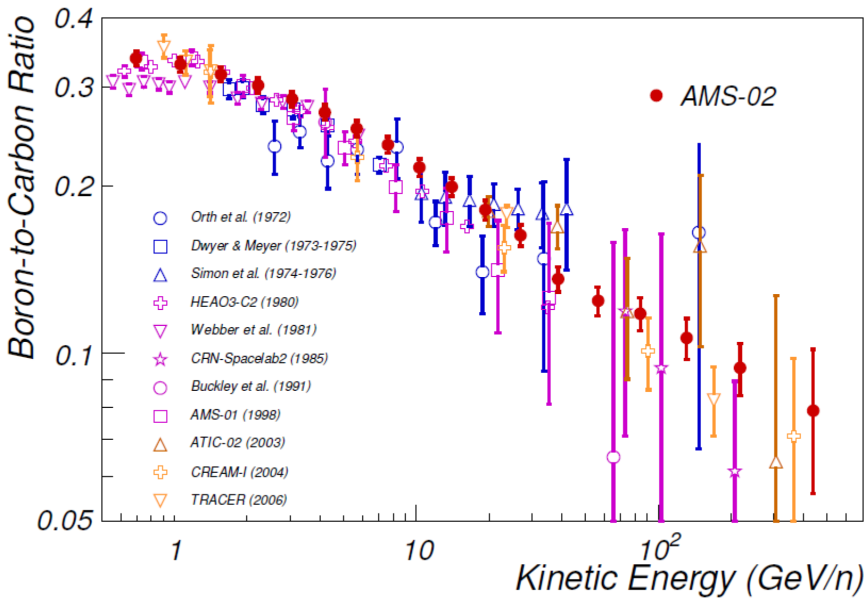

Figure 3.20: Boron to carbon ratio measured by AMS-02 compared with previous experiments [41].

CHAPTER 4

ANALYSIS

In this chapter high energy conversion mode photon analysis will be presented. High energy conversion mode photon events have one reconstructed Tracker track because the Silicon Tracker cannot spatially resolve two tracks of the resulting electron-positron pair. Motivation of this analysis is to use the ECAL for energy information, and the Tracker for angle information which is far better than that of the ECAL. A set of cuts to eliminate background events will be explained in detail. Then, the physics results will be discussed.

4.1 Event Selection

In order to determine the cuts which will be used in data, Monte Carlo (MC) samples are used. Energy range of the MC samples are: from $100\ GeV$ to $2000\ GeV$ for photons and electrons; and from $200\ GeV$ to $4000\ GeV$ for protons. ISS data used in this analysis covers the AMS-02 data from 19th of May, 2011 to 28th of February, 2014.

Resolution

For the energy bins in all plots, energy resolution of the ECAL is used which can be seen in Figure 4.1. Figure 4.2 shows the angular resolution of the ECAL. Resolution plots are obtained using photon MC sample between $5\ GeV$ and $100\ GeV$. The angular resolution is plotted by comparing the direction of the reconstructed ECAL shower with the truth value. The distribution of the difference between the reconstructed and truth angle value is fitted with a Gaussian. Energy resolution is obtained similarly by fitting the distribution of $(E_{rec} - E_{gen})/E_{gen}$.

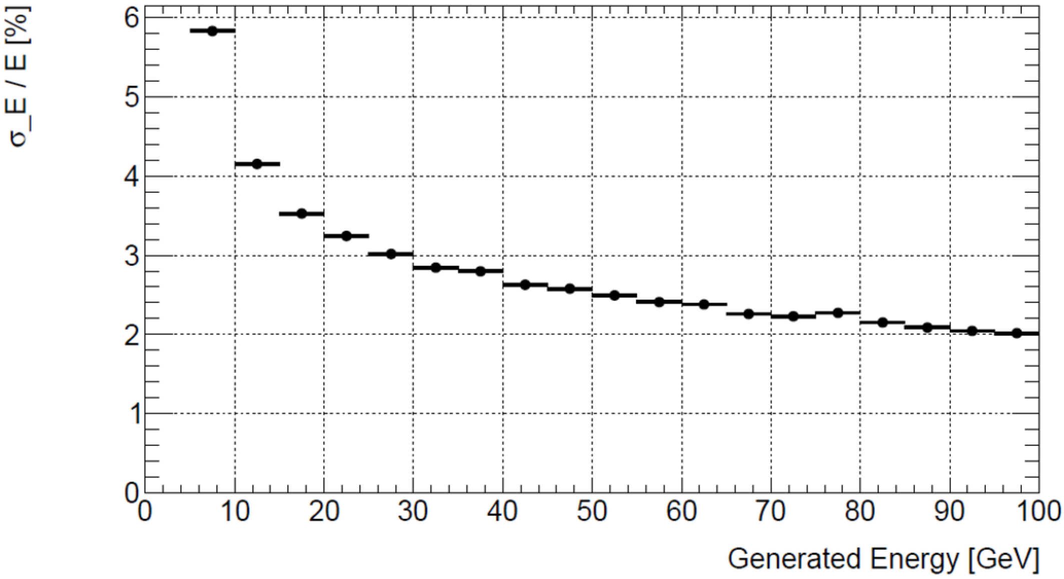

Figure 4.1: Energy resolution of the ECAL with respect to energy. It is derived using photon MC.

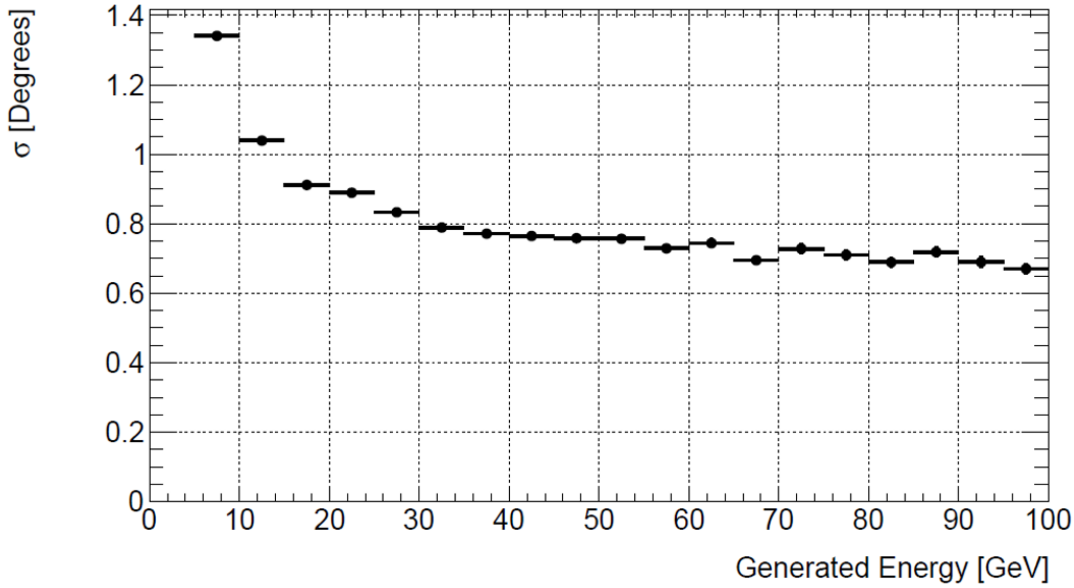

Figure 4.2: Angular resolution of the ECAL with respect to energy. It is derived using photon MC.

However the motivation of this analysis is to use angular resolution from the Tracker which is better than that of the ECAL. Angular resolution of the Tracker is only limited by the opening angle of e^+e^- pair and the multiple scattering.

Preselection

There are some data quality cuts which are necessary for the detector to work under optimum conditions. Two cuts are used to satisfy this. One of them is science run tag, and the other is live time. With the science run tag cut, events which are in the bad run list are not included in the selection. In South Atlantic Anomaly (SAA) region there is very high rate of particles because trapped low energy particles are closer to the surface of the Earth due to the shift of the axis of the magnetic dipole field from the center of the Earth [29]. To exclude data taken from SAA region, live time is required to be greater than 0.65.

Events which have single particle showers in the ECAL are required. The ECAL shower is required to start and exit (if the event is energetic enough to exit from the ECAL) in the ECAL fiducial volume. Fiducial volume cut rejects the events which have the particle shower within $2\ cm$ of the edge of the ECAL planes.

Tracker Track

Since converted photon events which have energies larger than $50\ GeV$ seems to have one Tracker track, a single track cut is applied. As seen in Figure 4.3, 10% of the MC photon events have single track. Most of the photon events in the sample do not have a Tracker track.

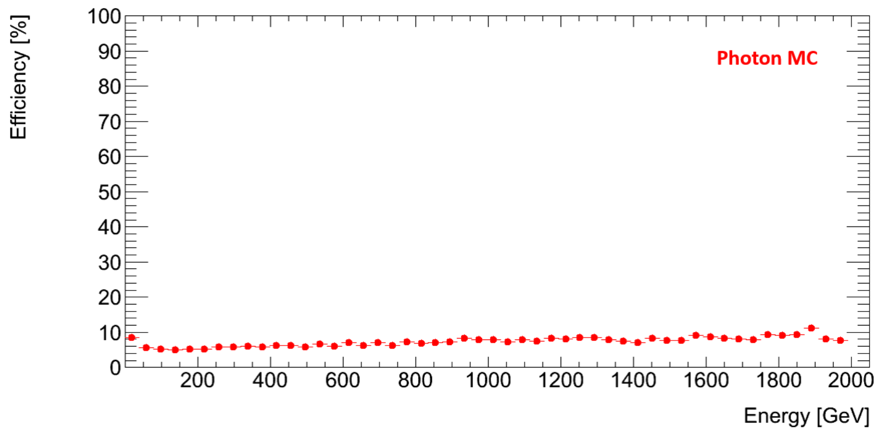

Figure 4.3: Efficiency versus reconstructed energy for single track cut.

It should be noted here that all the following efficiency plots are obtained after the cuts presented until here which are science run tag, live time, single shower, the ECAL fiducial volume, and the single track.

This single track is also required to have a chi-square value less than 10. Figure 4.4 shows the distribution of chi-square which is obtained using photon MC.

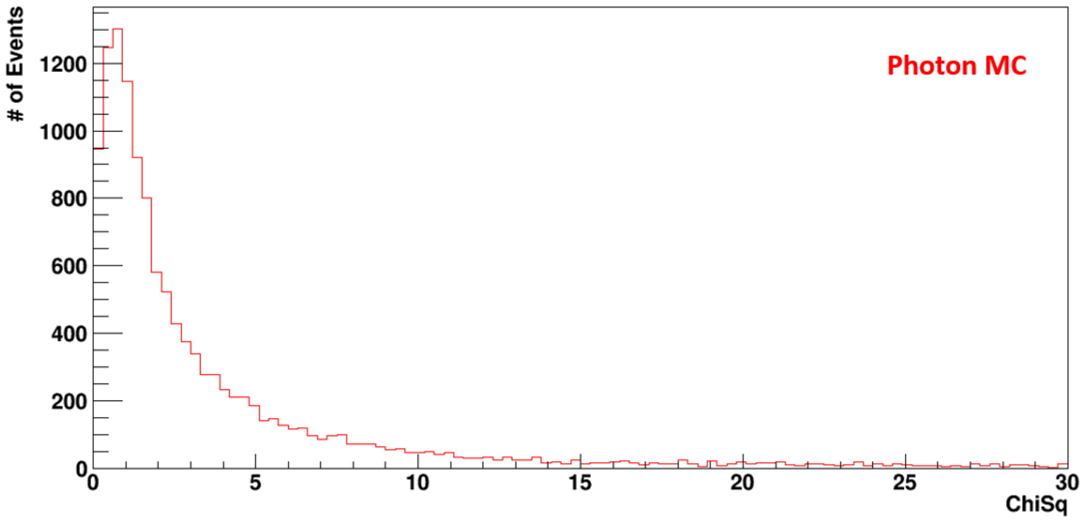

Figure 4.4: Chi-square distribution of photon MC. A loose cut is applied, tracks which have a chi-square value less than 10 are selected.

Tracker Charge

Protons have a dominant abundance in cosmic rays; therefore, they are the main background for several analyses. Moreover, for the high energy conversion mode analysis, electrons are also background events because many features of electrons and converted photons are similar, such as their Tracker tracks and ECAL shower shapes. Therefore, an efficient cut is required to reject also background electron events.

Although electron-positron pair seems to have one Tracker track in high energies, they give double contribution of charge deposition to the Silicon Tracker planes. Therefore, this variable can be used to select converted photons as they give a larger value of charge than 1. Figure 4.5 shows the charge values for photon, electron, proton, and helium MC samples. It can be seen that converted photons have a peak at 1.4 while electrons and protons have peaks at 1. Since energy deposition is proportional to the square root of Z, contributions from e^- and e^+ add up to give a peak at 1.4 instead of 2.

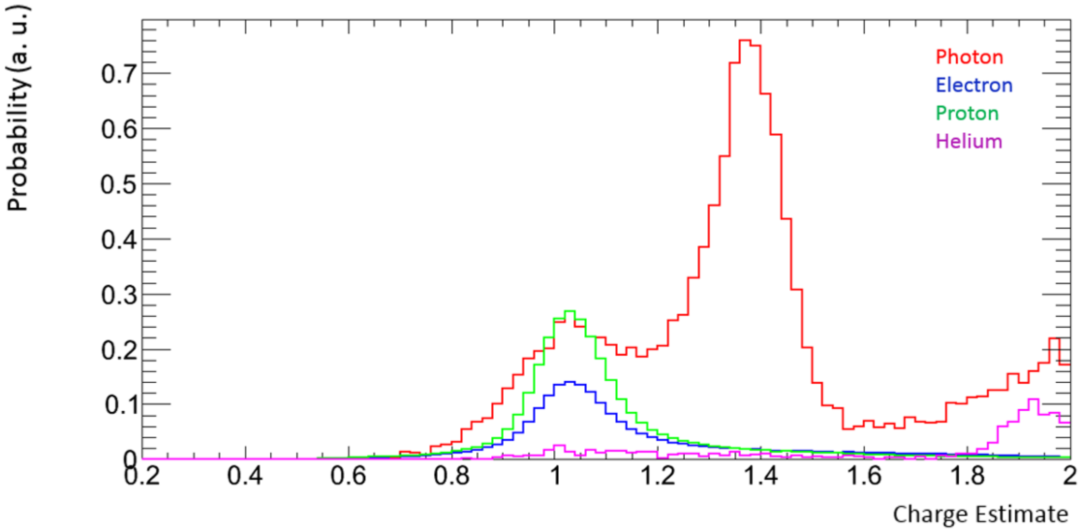

Figure 4.5: MC tracker charge values for photon, electron, proton, and helium; in red, blue, green, and purple, respectively. Electron and proton samples have a peak around 1, while converted photons have a peak around 1.4. Helium has a peak at 2 which is not the main background. A selection is applied between 1.2 and 1.8.

Figure 4.6 shows the charge value determined from all individual Tracker layers. Layer 9 gives more electron like charge value, hence it is excluded for the charge calculation.

The efficiency plots for charge larger than 1.2 and charge below 1.8 are shown in Figure 4.7 and Figure 4.8, respectively. As it can be seen in these plots, these cuts are two of the most effective cuts in the analysis.

Figure 4.9 shows the charge value for ISS data. The proton domination in cosmic rays can be seen in this figure.

TRD Geometrical Acceptance

To use a TRD hits cut which is important for this analysis, and will be explained next, events are required to be in the TRD geometrical acceptance. Figure 4.10 shows the efficiency of the cut using photon MC samples. The cut has almost 100% in all the energy range for MC events.

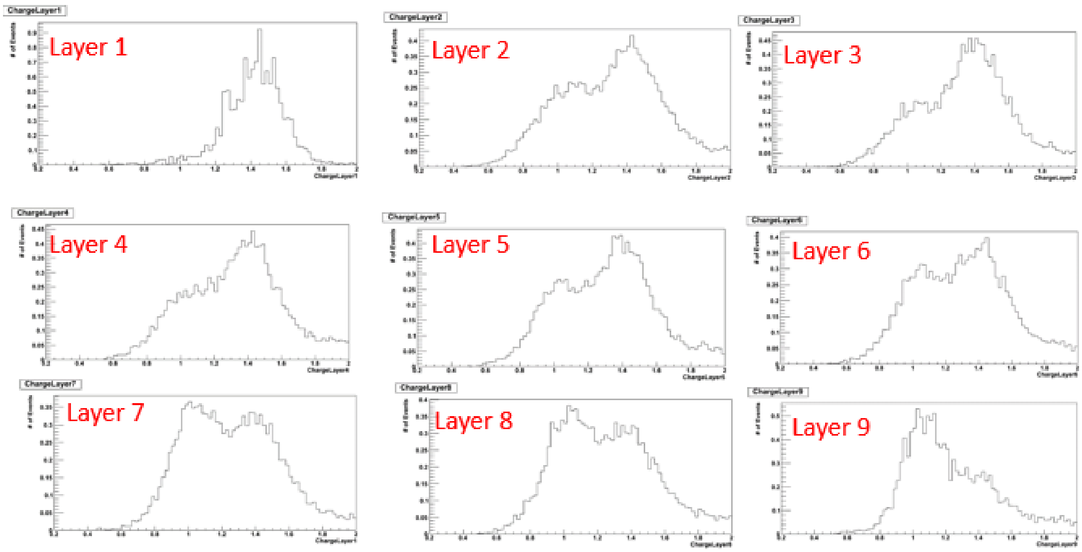

Figure 4.6: Photon MC charge information in different Tracker layers. While the layer number is increasing, the charge information becomes more electron like. In layer 9, most of the events have charge value of 1 which is incompatible with converted photons. For this reason, Layer 9 is excluded when calculating the charge value.

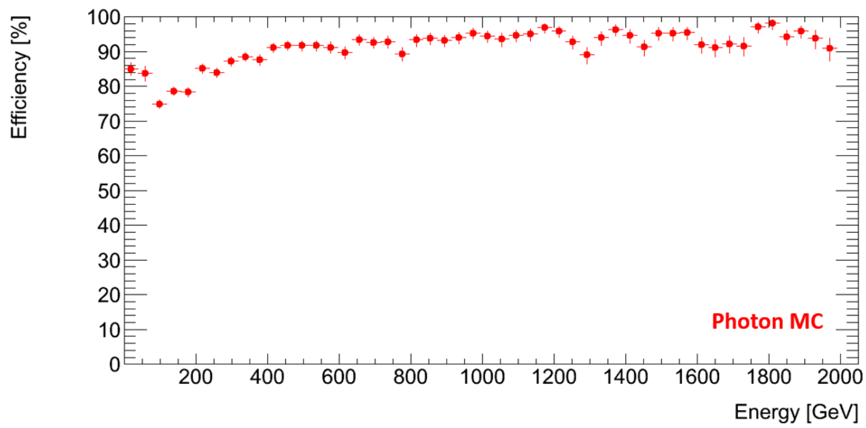

Figure 4.7: Efficiency versus reconstructed energy for charge larger than 1.2 cut.

TRD Hits

In the TRD, an electron have both energy deposition and TR contribution. Since converted photons consist of electron-positron pairs, in these type of events, both the energy deposition and TR contribution are doubled. However, one must be sure that these two particles come from an initial photon. To do this, events which have no TRD

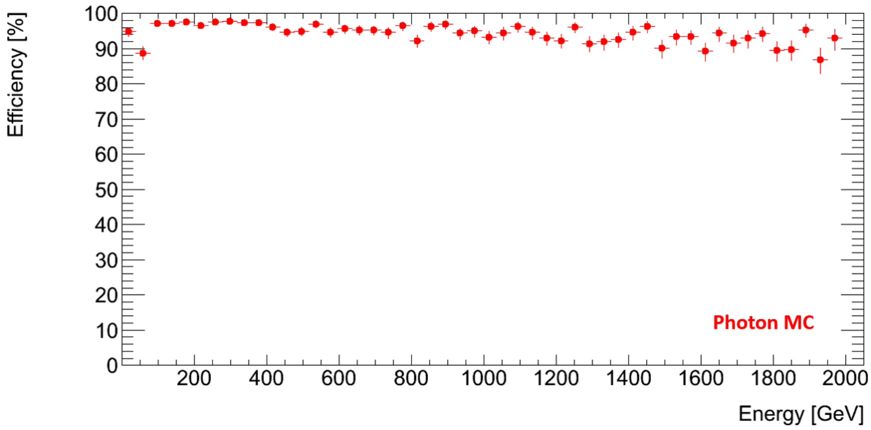

Figure 4.8: Efficiency versus reconstructed energy for charge below 1.8 cut.

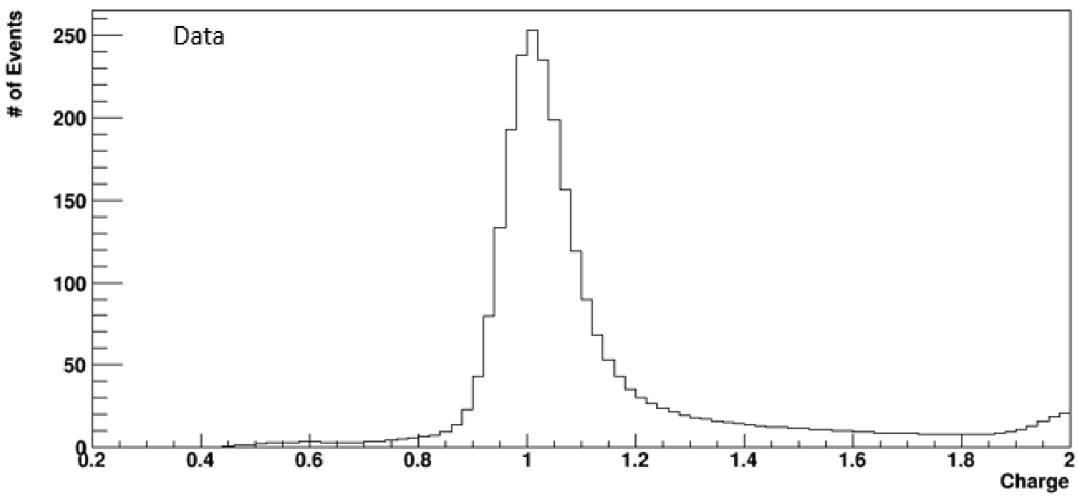

Figure 4.9: Tracker charge value of ISS data. Proton domination in cosmic rays can be seen in the peak around 1. Between 1.2 and 1.8 is selected for converted photon signal.

hits in first 5 layers are selected. Determining the number 5 depends on two things. First, the number of layers which must have no hits should be minimized, because as the number increases, the number of layers from which the energy deposition and the TR contribution can be measured decreases accordingly. Second one comes from the structure of the TRD. In the TRD, first 4 layers are orthogonal to next 12 layers. Then, adding an orthogonal layer increases the probability of a photon not to miss the straw tubes. Figure 4.11 shows the efficiency of this cut which is around 60% up to $2\,TeV$.

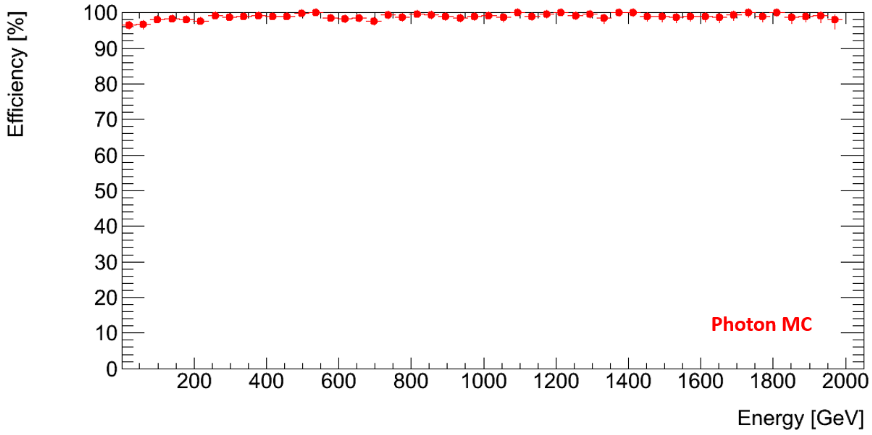

Figure 4.10: Efficiency versus reconstructed energy for TRD geometrical acceptance cut.

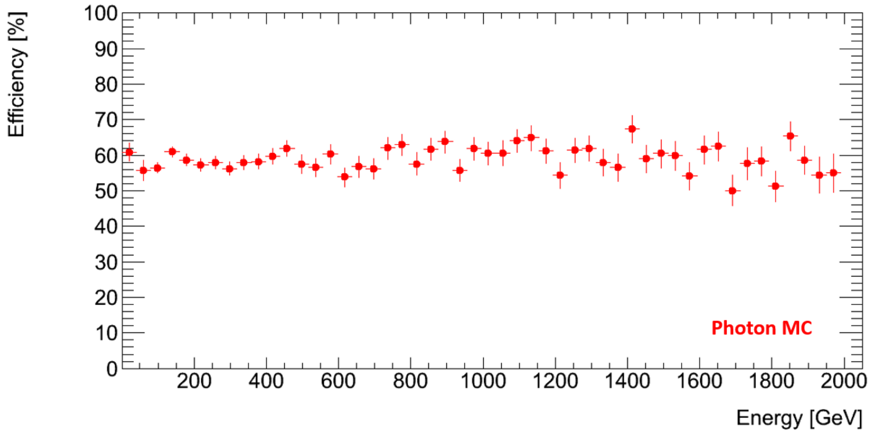

Figure 4.11: Efficiency versus reconstructed energy for no hits in TRD first 5 layers cut.

Cos(z) of the ECAL Shower

By the ECAL shower shape, it can be determined whether an event is downward or upward going. Figure 4.12 shows the $cos(z)$ of the ECAL shower from photon MC. Almost all events are around -1 which are the selected downward going particles. Events which have $cos(z) > 0$ of the ECAL shower which can be seen in Figure 4.13 are the upward going particles, and are rejected.

ECAL Shower - Tracker Track Spatial Matching

Although there is a cut such as $cos(z)$ of ECAL shower, there are still misreconstructed upward going particles. These type of events characteristically do not have spatially matched Tracker track and the ECAL shower. In order to reject these type

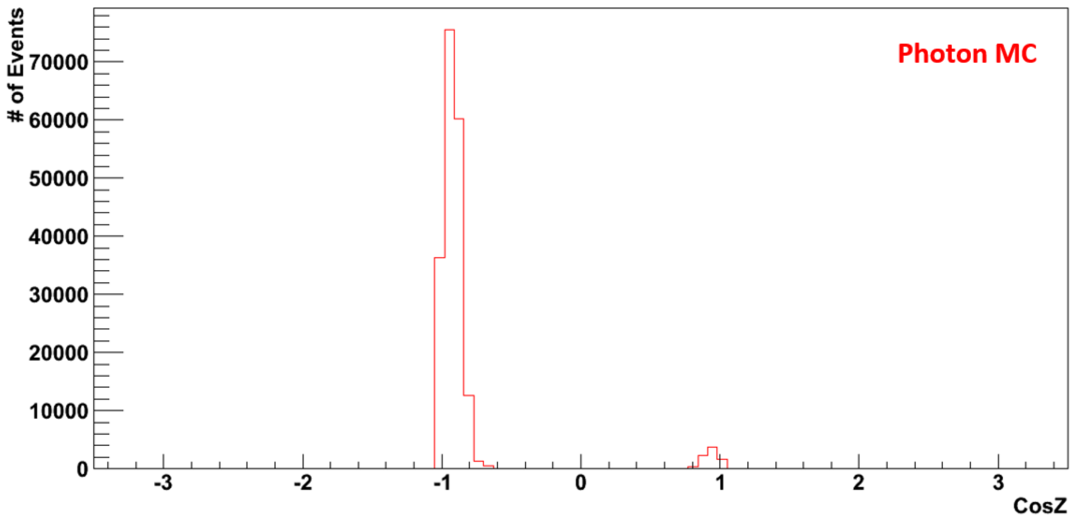

Figure 4.12: $cos(z)$ of ECAL shower value derived by using photon MC. Downward going events have $cos(z)$ value of -1.

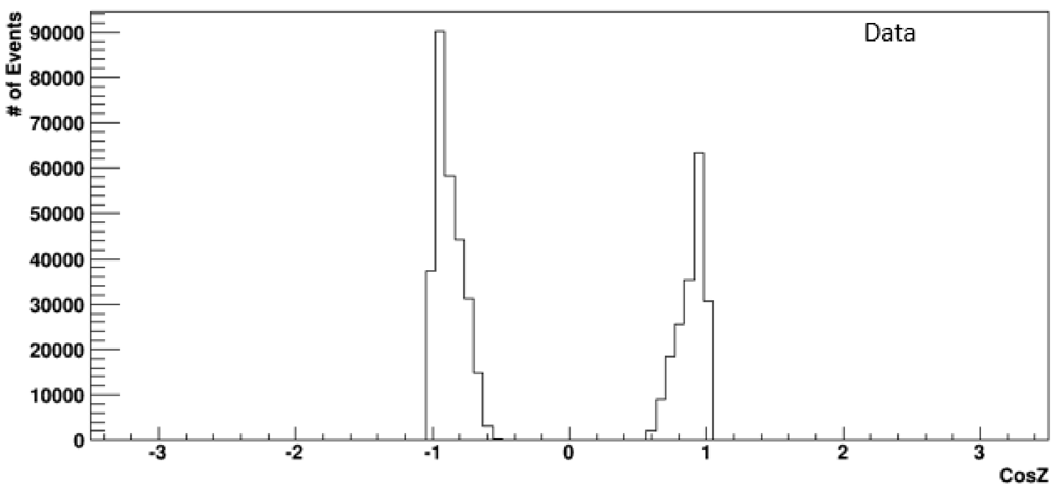

Figure 4.13: $cos(z)$ of ECAL shower for ISS data. Events at 1 are undesired upward going particles. Then, events at -1 are selected.

of events, a $5\ cm$ spatial matching condition is applied. Efficiency of this cut changes between 50% and 70% with energy as shown in Figure 4.14.

Energy over Momentum

This cut serves similar purpose with the matching cut. In some cases upward going particles are reconstructed as downward going, and after shower, which is started at

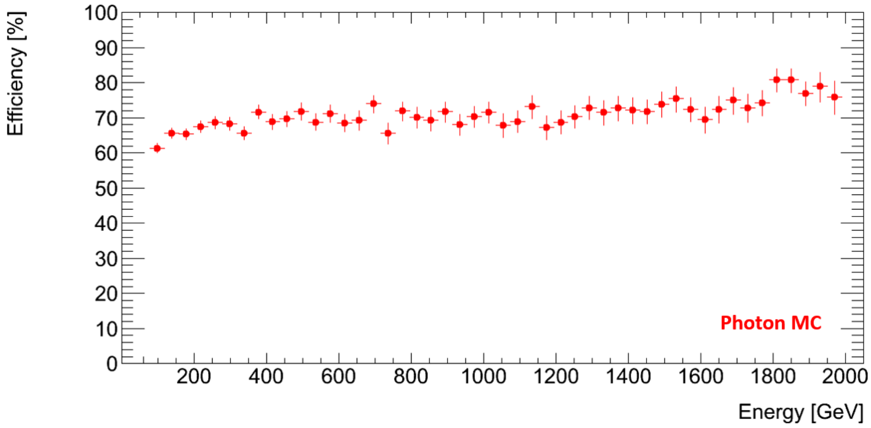

Figure 4.14: Efficiency versus reconstructed energy for (ECAL Shower - Tracker Track) < $5\ cm$ cut.

the bottom of the ECAL, secondary particles which have low momentum give tracks in the Tracker. Therefore, the rigidity value measured by the Tracker and the energy value measured by the ECAL do not match. To reject this kind of events, a cut to E/p is required. Energy is obtained from the ECAL, and it is divided by the momentum which is obtained from the Tracker. Events which have energy over momentum value larger than 30 are rejected which can be seen in Figure 4.15.

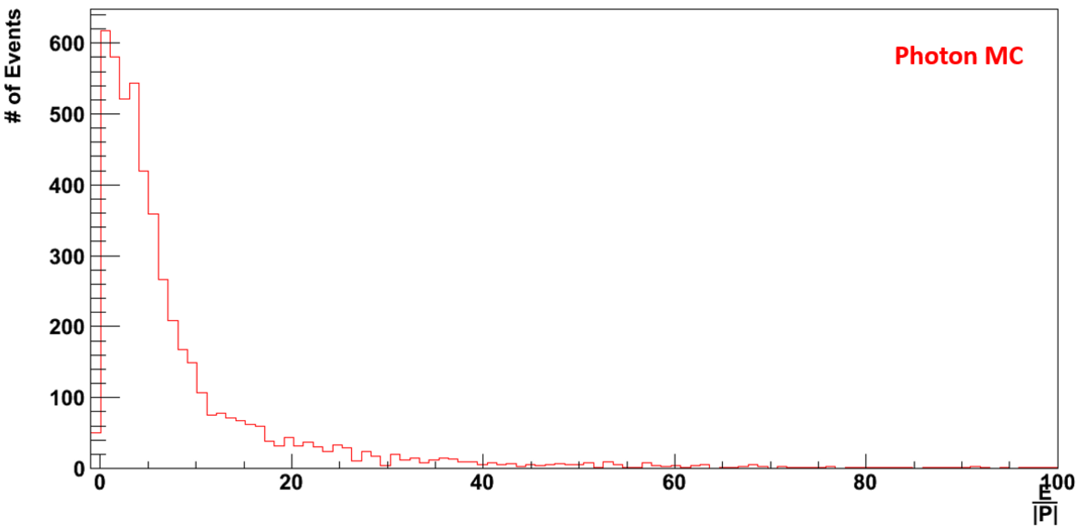

Figure 4.15: E/p value for photon MC. Events which have $E/p < 30$ are selected.

Figure 4.16 shows the efficiency for $E/p < 30$ cut with respect to energy. Efficiency of this cut is nearly flat around 85%.

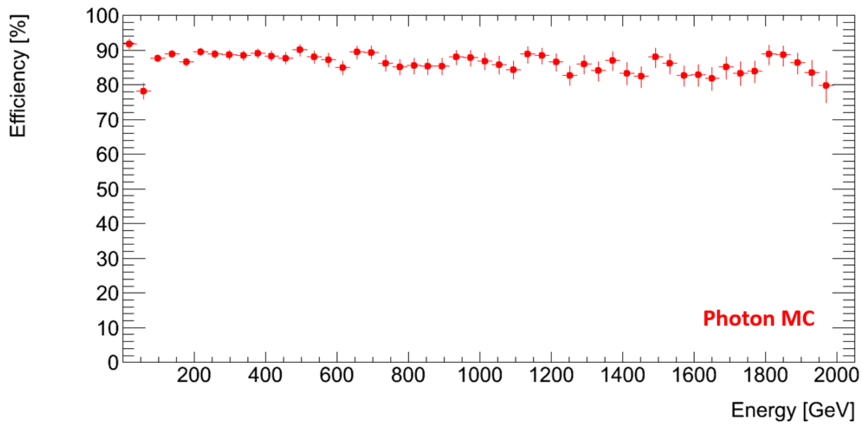

Figure 4.16: Efficiency versus reconstructed energy for $E/p < 30$ cut.

ECAL BDT

The ECAL Boosted Decision Tree (BDT) is a variable uses shower features of events to eliminate the most abundant cosmic ray components, protons. Most of the protons behave as MIPs, and do not produce a shower in the ECAL. Then, the fraction of energy deposition in each layer allows for an effective separation between protons and electrons. Thus, if protons interact with the ECAL, they give hadronic showers which are different than electromagnetic showers. Then, with the help of these different shower profiles, the BDT is trained. With the match between energy and momentum, the rejection power of the BDT rises to about 10^4.

Figure 4.17 shows the BDT variable for photon, electron, and proton MC samples. Protons have a peak at -1, while electrons and converted photons have peaks at 1. Events which have the BDT value larger than 0.5 are selected which is the same as lepton analyses.

It can be seen in Figure 4.18 that the BDT cut has an efficiency between 60% and 90% up to 2 TeV.

Figure 4.19 shows the BDT value for ISS data. Most of the events are at -1 value which is because of the proton abundance in cosmic rays.

Figure 4.20 shows an MC photon event which passes all the cuts in the event selection. There are no hits in the first layers of the TRD, but there are TRD clusters in the following layers, i.e., the photon converts in the TRD. The resultant e^+ and e^- are so

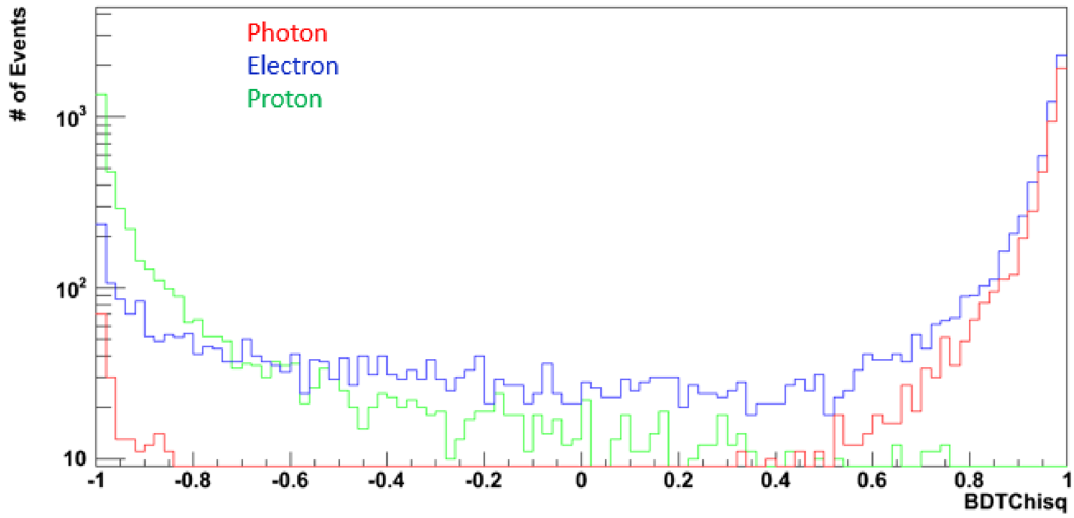

Figure 4.17: MC ECAL BDT values for photon, electron, and proton; in red, blue, and green, respectively. Protons has a peak at -1 while converted photons and electron have peaks at 1. A selection is applied for events larger than 0.5. This is the most powerful cut to eliminate proton background.

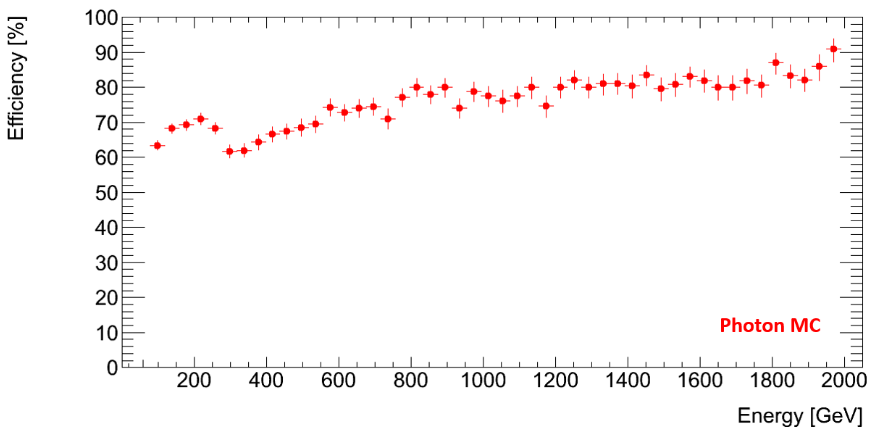

Figure 4.18: Efficiency versus reconstructed energy for the ECAL BDT > 0.5 cut.

close to each other that the Tracker reconstructs only one track. Then the event gives an ECAL shower.

4.2 Results and Discussion

MC study shows that all the cuts except the single track cut have at least 50% efficiencies. Thus, efficiencies does not vary much with increasing energy. And the

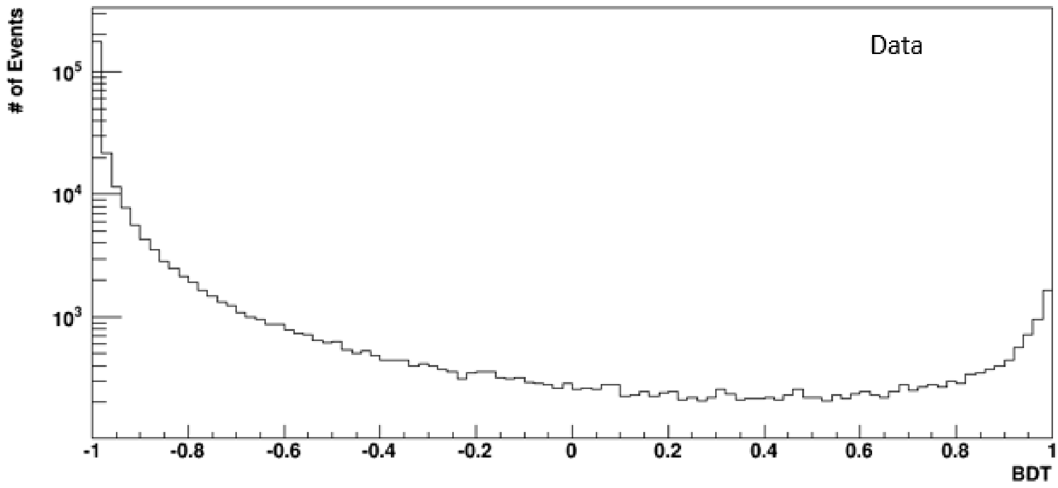

Figure 4.19: The ECAL BDT value of ISS data. Events at -1 are protons. Events which have a BDT value below 0.5 are rejected.

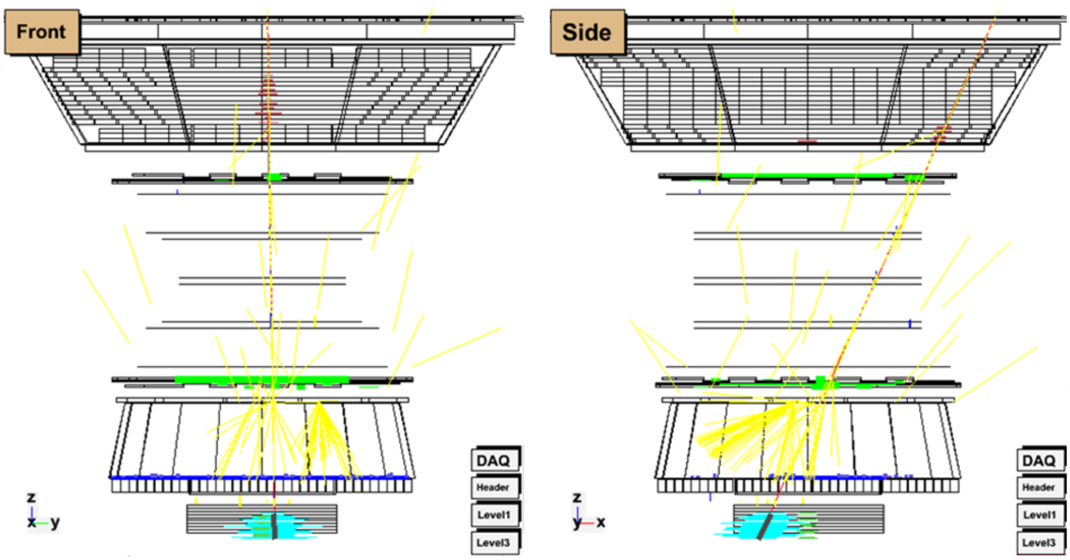

Figure 4.20: A front and side view of AMS-02 event display which shows a high energy conversion mode MC photon event which passes all the cuts in the event selection.

small variations in efficiencies have increasing trend which is favorable because the analysis is optimized for high energies. Three most important cuts are the TRD hits for e rejection, the Tracker charge for e and p rejection, and the ECAL BDT for p rejection.

After all the cuts have been applied there are no events left in AMS-02 data, with the energy larger than $100\ GeV$ which is the main energy regime for the analysis. Although the low statistics is expected, the objective was to measure few clean converted photon events which have energies larger than $100\ GeV$. Figure 4.21 shows the expected spectrum derived from Fermi power law fit which can be seen in Figure 2.8 multiplied by AMS-02 exposure ($9.5 \times 10^7\ s$), AMS-02 acceptance ($0.4\ m^2 sr$), and analysis efficiencies.

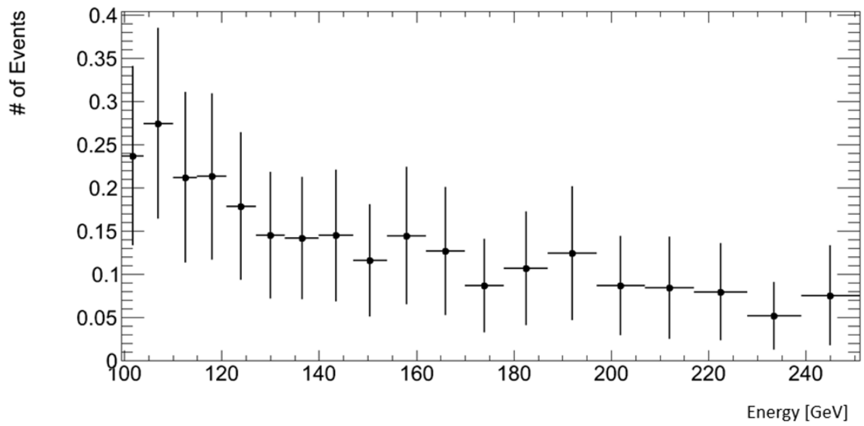

Figure 4.21: Expected number of events derived using Fermi power law fit in Figure 2.8.

CHAPTER 5

CONCLUSION

In this thesis historical development and observational evidences of dark matter were reviewed. Theoretical predictions for the particle nature of dark matter, and the most favored models were introduced. Direct detection, accelerator searches, and indirect detection efforts to obtain a dark matter particle signature were explained. The most sophisticated astroparticle physics detector in space up to now, AMS-02, which collected more than 50 billion events was explained.

Motivation of the analysis was to select high energy photons without the limitation of the angular resolution of the ECAL which is inevitable in the calorimetric mode analysis. This analysis aimed to select high energy conversion mode photons where the angle information is obtained from the Silicon Tracker and the energy information, from the ECAL. In order to determine the cuts which were applied later to the ISS data, high energy MC samples for photons, electrons, and protons were used. Although the expected number of events were low, the goal was to measure a few converted photon events larger than $100\ GeV$. None were observed.

While this investigation yielded no candidates with current statistics, this analysis can be developed further by successor group members, and with increasing statistics, it can produce candidate events in the future.

REFERENCES

[1] G. Aad et al. Search for supersymmetry using final states with one lepton, jets, and missing transverse momentum with the ATLAS detector in $\sqrt{s} = 7$ TeV pp. *Phys.Rev.Lett.*, 106:131802, 2011, arXiv:hep-ex/1102.2357.

[2] G. Aad et al. Search for direct production of charginos, neutralinos and sleptons in final states with two leptons and missing transverse momentum in pp collisions at $\sqrt{s} = 8$ TeV with the ATLAS detector. *JHEP*, 1405:071, 2014, arXiv:hep-ex/1403.5294.

[3] M. Aartsen et al. IceCube Search for Dark Matter Annihilation in nearby Galaxies and Galaxy Clusters. *Phys.Rev.*, D88(12):122001, 2013, arXiv:astro-ph.HE/1307.3473.

[4] Ackermann et al. Fermi LAT search for dark matter in gamma-ray lines and the inclusive photon spectrum. *Phys.Rev.D*, 86(2):022002, July 2012, arXiv:astro-ph.HE/1205.2739.

[5] M. Ackermann et al. Measurement of separate cosmic-ray electron and positron spectra with the Fermi Large Area Telescope. *Phys.Rev.Lett.*, 108:011103, 2012, arXiv:astro-ph.HE/1109.0521.

[6] P. Ade et al. Planck 2013 results. I. Overview of products and scientific results. 2013, arXiv:astro-ph.CO/1303.5062.

[7] P. Ade et al. Planck 2013 results. XV. CMB power spectra and likelihood. 2013, arXiv:astro-ph.CO/1303.5075.

[8] O. Adriani et al. An anomalous positron abundance in cosmic rays with energies 1.5-100 GeV. *Nature*, 458:607–609, 2009, arXiv:astro-ph/0810.4995.

[9] M. Aguilar et al. Cosmic-ray positron fraction measurement from 1 to 30 GeV with AMS-01. *Physics Letters B*, 646(4):145 – 154, 2007.

[10] M. Aguilar et al. First Result from the Alpha Magnetic Spectrometer on the International Space Station: Precision Measurement of the Positron Fraction in Primary Cosmic Rays of 0.5–350 GeV. *Phys.Rev.Lett.*, 110:141102, 2013.

[11] E. Aprile et al. Dark Matter Results from 225 Live Days of XENON100 Data. *Phys.Rev.Lett.*, 109:181301, 2012, arXiv:astro-ph.CO/1207.5988.

[12] S. Barwick et al. Measurements of the cosmic ray positron fraction from 1-GeV to 50-GeV. *Astrophys.J.*, 482:L191–L194, 1997, arXiv:astro-ph/9703192.

[13] P. Battinelli and S. Demers. The C star population of DDO 190. *A&A*, 447:473–480, Feb. 2006.

[14] J. Beatty, A. Bhattacharyya, C. Bower, S. Coutu, M. DuVernois, et al. New measurement of the cosmic-ray positron fraction from 5 to 15-GeV. *Phys.Rev.Lett.*, 93:241102, 2004, arXiv:astro-ph/0412230.

[15] K. Begeman, A. Broeils, and R. Sanders. Extended rotation curves of spiral galaxies: Dark haloes and modified dynamics. *Mon.Not.Roy.Astron.Soc.*, 249:523, 1991.

[16] B. Beltran et al. Search for solar axions: The CAST experiment at CERN. *PoS*, HEP2005:022, 2006, arXiv:hep-ex/0507007.

[17] C. L. Bennett et al. Nine-year Wilkinson Microwave Anisotropy Probe (WMAP) Observations: Final Maps and Results. *Astrophys.J.Suppl.S.*, 208:20, Oct. 2013, arXiv:astro-ph.CO/1212.5225.

[18] B. Bertucci on behalf of the AMS Collaboration. Precision measurement of the $e^+ + e^-$ spectrum with AMS. *33rd International Cosmic Ray Conference, The Astroparticle Physics Conference*, 2013.

[19] H. Bethe and W. Heitler. On the Stopping of fast particles and on the creation of positive electrons. *Proc.Roy.Soc.Lond.*, A146:83–112, 1934.

[20] M. Boezio, P. Carlson, T. Francke, N. Weber, M. Suffert, et al. The Cosmic-Ray Electron and Positron Spectra Measured at 1 AU during Solar Minimum Activity. *Astrophys.J.*, 532:653–669, 2000.

[21] N. W. Boggess et al. The COBE mission - Its design and performance two years after launch. *Astrophys.J.*, 397:420–429, Oct. 1992.

[22] M. Buénerd. The RICH counter of the AMS experiment. *Nucl. Instrum. Meth.*, A502:158–162, 2003.

[23] I. Buesching, O. de Jager, M. Potgieter, and C. Venter. A Cosmic Ray Positron Anisotropy due to Two Middle-Aged, Nearby Pulsars. 2008, arXiv:astro-ph/0804.0220.

[24] W. J. Burger. The AMS silicon tracker. *Nucl.Phys.Proc.Suppl.*, 113:139–146, 2002.

[25] J. Casaus on behalf of the AMS Collaboration. Determination of the positron anisotropy with AMS. *33rd International Cosmic Ray Conference, The Astroparticle Physics Conference*, 2013.

[26] V. Choutko on behalf of the AMS Collaboration. Precision measurement of the cosmic ray helium flux with AMS experiment. *33rd International Cosmic Ray Conference, The Astroparticle Physics Conference*, 2013.

[27] J. Clem and P. Evenson. Cosmic ray positron fraction observations during the A-magnetic solar minimum. *Proc. 30th ICRC Merida*, 2007.

[28] D. Clowe, M. Bradac, A. H. Gonzalez, M. Markevitch, S. W. Randall, et al. A direct empirical proof of the existence of dark matter. *Astrophys.J.*, 648:L109–L113, 2006, arXiv:astro-ph/0608407.

[29] A. Contin and D. Grandi. South atlantic anomaly definition, June 2012.

[30] T. Daylan. Photon proton separation using Alpha Magnetic Spectrometer 02, July 2013.

[31] B. Demirköz. A transition radiation detector and gas supply system for AMS. Master's thesis, Massachusetts Institute of Technology, 2004.

[32] S. Haino on behalf of the AMS Collaboration. Precision measurement of the proton flux with AMS. *33rd International Cosmic Ray Conference, The Astroparticle Physics Conference*, 2013.

[33] H. Hirayama. Lecture note on photon interactions and cross sections. Internal 2000-10, KEK, November 2000.

[34] G. Jungman, M. Kamionkowski, and K. Griest. Supersymmetric dark matter. *Physics Reports*, 267(5–6):195 – 373, 1996.

[35] V. Khachatryan et al. Searches for electroweak production of charginos, neutralinos, and sleptons decaying to leptons and W, Z, and Higgs bosons in pp collisions at 8 TeV. 2014, arXiv:hep-ex/1405.7570.

[36] A. Kounine on behalf of the AMS Collaboration. Precision measurement of the positron fraction in primary cosmic rays of 0.5-350 GeV. *33rd International Cosmic Ray Conference, The Astroparticle Physics Conference*, 2013.

[37] B. T. Le. *Search for extra dimensions in the diphoton channel with ATLAS experiment at LHC*. PhD thesis, Université De Grenoble, 2013.

[38] M. S. Longair. *High Energy Astrophysics*. Cambridge University Press, 2011.

[39] D. Mueller and K.-K. Tang. Cosmic-ray positrons from 10 to 20 GeV - A balloon-borne measurement using the geomagnetic east-west asymmetry. *Astrophys.J.*, 312:183–194, Jan. 1987.

[40] A. Oliva. *High Charge Cosmic Rays Measurement with the AMS-02 Silicon Tracker*. PhD thesis, Universita degli studi di Perugia, 2006.

[41] A. Oliva on behalf of the AMS Collaboration. Precision measurement of the cosmic ray boron-to-carbon ratio with AMS. *33rd International Cosmic Ray Conference, The Astroparticle Physics Conference*, 2013.

[42] R. Peccei and H. R. Quinn. CP Conservation in the Presence of Instantons. *Phys.Rev.Lett.*, 38:1440–1443, 1977.

[43] F. Pilo. *Diffuse Gamma Ray emission detection with the AMS-02 electromagnetic calorimeter*. PhD thesis, Universita degli studi di Siena, 2005.

[44] V. Rubin, N. Thonnard, and J. Ford, W.K. Rotational properties of 21 SC galaxies with a large range of luminosities and radii, from NGC 4605 /R = 4kpc/ to UGC 2885 /R = 122 kpc/. *Astrophys.J.*, 238:471, 1980.

[45] V. C. Rubin and W. K. Ford, Jr. Rotation of the Andromeda Nebula from a Spectroscopic Survey of Emission Regions. *Astrophys.J.*, 159:379–403, 1970.

[46] T. Saab. An Introduction to Dark Matter Direct Detection Searches & Techniques. 2012, arXiv:physics.ins-det/1203.2566.

[47] S. Schael on behalf of the AMS Collaboration. Precision measurements of the electron spectrum and the positron spectrum with ams. *33rd International Cosmic Ray Conference, The Astroparticle Physics Conference*, 2013.

[48] The AMS Collaboration. http://ams.cern.ch.

[49] The AMS Collaboration. AMS on ISS Construction of a particle physics detector on the International Space Station. *AMS Note*, 2004.

[50] M. Verducci. Hidden Valley search at ATLAS. *J.Phys.Conf.Ser.*, 335:012068, 2011.

[51] F. Zwicky. On the Masses of Nebulae and of Clusters of Nebulae. *Astrophys.J.*, 86:217–246, 1937.